nature structural & molecular biology

Article

https://doi.org/10.1038/s41594-024-01255-0

# SCAF1 drives the compositional diversity of mammalian respirasomes

Received: 25 July 2023

Accepted: 16 February 2024

Published online: 4 April 2024

Check for updates

Irene Vercellino [1,2] & Leonid A. Sazanov [1]

Supercomplexes of the respiratory chain are established constituents of the oxidative phosphorylation system, but their role in mammalian metabolism has been hotly debated. Although recent studies have shown that different tissues/organs are equipped with specific sets of supercomplexes, depending on their metabolic needs, the notion that supercomplexes have a role in the regulation of metabolism has been challenged. However, irrespective of the mechanistic conclusions, the composition of various high molecular weight supercomplexes remains uncertain. Here, using cryogenic electron microscopy, we demonstrate that mammalian (mouse) tissues contain three defined types of 'respirasome', supercomplexes made of CI, $CIII_2$ and CIV. The stoichiometry and position of CIV differs in the three respirasomes, of which only one contains the supercomplex-associated factor SCAF1, whose involvement in respirasome formation has long been contended. Our structures confirm that the 'canonical' respirasome (the C-respirasome, $CICIII_2CIV$) does not contain SCAF1, which is instead associated to a different respirasome (the CS-respirasome), containing a second copy of CIV. We also identify an alternative respirasome (A-respirasome), with CIV bound to the 'back' of CI, instead of the 'toe'. This structural characterization of mouse mitochondrial supercomplexes allows us to hypothesize a mechanistic basis for their specific role in different metabolic conditions.

## Supercomplexes of mammalian tissues

Respiratory chain complexes CI (NADH-ubiquinone oxidoreductase), $CIII_2$ (cytochrome $bc_1$ oxidoreductase) and CIV (cytochrome *c* oxidase) associate in the mitochondrial membrane to form supercomplexes (SCs) of defined stoichiometry[1]. SCs $CICIII_2CIV$ (also known as respirasome[2–4]), $CICIII_2$[5] and $CIII_2CIV$[6] have been structurally defined and a low-resolution map of a megacomplex $CI_2CIII_2CIV_2$[7] was reported. Functionally, SCs were shown to boost electron transfer efficiency[6], and provide mutual regulation of the complexes' assembly, stability and activity[5,8–12]. Additionally, the distribution of SCs across cell types, tissues and organs was linked to relevant implications in cancer[13–16], diabetes[17], exercise performance[18–20] (albeit with some controversy[21]), aging[22–24] and reactive oxygen species production[25,26]. An important regulator of SC composition is the supercomplex-associated factor SCAF1, or isoform COX7A2L of CIV subunit COX7A. SCAF1 is required for the formation of SC $CIII_2CIV$[27], as it structurally joins CIV and $CIII_2$[6]. Earlier studies in different species indicated that SCAF1 can be identified in a fraction of respirasomes[27,28]. Nevertheless, respirasomes were still present in SCAF1-knockout models[28–30], creating a controversy over SCAF1 role. Structural characterization of the major species of respirasome, $CICIII_2CIV$, henceforth referred to as the C-respirasome (where C stands for canonical or COX7A1/2-containing) unequivocally demonstrated that it does not contain SCAF1 (refs. 6,31). Heart-derived C-respirasome harbors muscle-specific isoform COX7A1 (ref. 6), whereas C-respirasome from kidney contains generally expressed COX7A2 (ref. 31).

[1]Institute of Science and Technology Austria, Klosterneuburg, Austria. [2]Present address: Forschungszentrum Jülich GmbH, Jülich, Germany.
e-mail: sazanov@ist.ac.at

https://doi.org/10.1038/s41594-024-01255-0

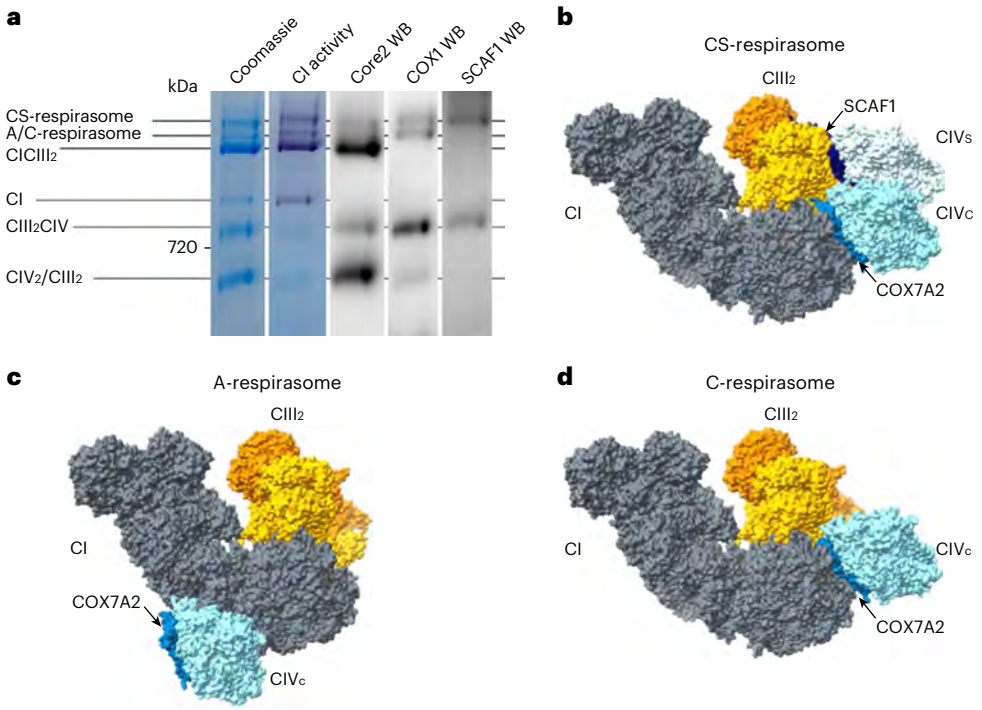


**Fig. 1 | SCs of mouse mitochondria. a**, BN-PAGE of purified liver CD1 mitochondria, stained or decorated as indicated above the lanes. The details on the staining can be found in Methods. The different species are indicated on the left for guidance. The experiment was repeated at least three times independently with similar results. **b**–**d**, Structures of the SCs described in this manuscript: CS-respirasome (**b**), A-respirasome (**c**) and C-respirasome (**d**). Each model is shown with surface representation and complexes are colored as follows: CI is gray, $CIII_2$ is yellow and orange (to distinguish the two protomers), $CIV_C$ is cyan, $CIV_S$ is ice, SCAF1 is dark blue and COX7A2 is light blue. The color code is maintained throughout, unless stated otherwise.

Recently SCAF1 was shown to drive metabolic rewiring in human cells[32], mouse models and humans[33], ascribed to changes in high molecular weight (HMW, about 1.7 MDa) areas of native gels, where respirasomes run. The re-expression of SCAF1 in C57BL/6J mice (otherwise lacking functional SCAF1) led to the appearance of specific HMW species[33] and the analysis of COX7A2 versus SCAF1-knockout in cultured human cells identified two putative types of respirasome (then dubbed C- and S-respirasomes, containing COX7A1/2 and SCAF1, respectively), with the S-respirasome being of slightly higher molecular weight than the C-respirasome[32]. C-respirasomes were associated with more efficient respiration[32,33], and S-respirasomes with glycolysis[32].

These results point toward multiple 'respirasomes' existing in mammals, some of which assemble via SCAF1, but their identity so far remained enigmatic. S-respirasomes could run slower than C-respirasomes on native gels due to additional protein components, or due to their different spatial arrangement. Without clear knowledge of their architecture, the molecular mechanism underlying the observed effects[32,33] in human and mice cannot be addressed. We thus set to (1) determine the atomic structures of the uncharacterized non-canonical respirasomes, and (2) identify their patterning and composition in ovine hearts and mouse tissues (brain, liver, kidney and heart), from both the wild-type strain CD1 and the SCAF1-mutant C57BL/6J.

## Multiple respirasomes exist in mice

Blue native polyacrylamide gel electrophoresis (BN-PAGE) can lead to crowded patterns, especially at HMW where the gel provides low resolution but most SCs reside: we thus employed ion exchange chromatography to partially separate the components of the solubilized mitochondrial membranes (Extended Data Fig. 1a,b). This method enabled us to separate ATP synthase (peak 1 fraction in Extended Data Fig. 1a) and individual CIV (peak 2) from the rest of respiratory complexes, leading to a clearer pattern of bands at HMW (peak 3). The distribution of HMW species differs across tissues and strains/species, but there are clear trends (Extended Data Fig. 2). First, CD1 brains, livers and kidneys (Fig. 1a and Extended Data Fig. 2b–d, Coomassie) have three main HMW SCs, of which the top and bottom are predominant, while the intermediate is less abundant. According to in-gel activity and western blots, the top band containing SCAF1, CI, $CIII_2$ and CIV is not present in C57BL/6J samples (Extended Data Fig. 2g–i), probably representing the S-respirasome. The bottom band contains only CI and $CIII_2$, representing $CICIII_2$. The middle band contains CI, $CIII_2$ and CIV, but no SCAF1, probably representing the C-respirasome. Thus, in brains, livers and kidneys of wild-type mice the C-respirasome is a minor species, whereas $CICIII_2$ and S-respirasome dominate. In the heart the proportion of C-respirasome increases (Extended Data Fig. 2a), although in all mouse samples $CICIII_2$ is the main HMW SC. By contrast, in ovine hearts (Extended Data Fig. 2e) the canonical respirasome is the predominant species, followed by $CICIII_2$ (in agreement with previously solved structures[3,6]) and very little S-respirasome. These patterns of SC distribution in tissues are consistent with the proposed association[32] of C-respirasomes with efficient respiration (heart) and S-respirasomes with enhanced glycolysis (brains, livers and kidneys).

## Structures of three different respirasomes

Because our analysis, in agreement with biochemical findings[32,33], identified a SCAF1-containing 'respirasome', we prepared cryogenic electron microscopy (cryo-EM) samples from HMW SCs from CD1 mice liver and brain and solved their structures (Fig. 1, Table 1 and Extended Data Figs. 3–5). Liver, being the largest collected organ, with the highest yield of purified SCs, was used for structural studies. The rationale for analyzing brain was two-pronged: (1) to visualize the brain-specific isoform of subunit NDUFV3 in CI (see 'Complex I conformation' section), and (2) to confirm whether the biochemically conserved bands observed by BN-PAGE (Extended Data Fig. 2) would correspond structurally to the SCs defined in liver. Although the HMW SCs could not

https://doi.org/10.1038/s41594-024-01255-0

**Table 1 | Cryo-EM collection, maps and model statistics of the SCs**

| | #1 CS-respirasome $CIC III_2 CIV_2$ (PDB 8PW5) | #2 C-respirasome $CIC III_2 CIV$ (PDB 8PW6) | #3 A-respirasome $CIC III_2 CIV$ (PDB 8PW7) |
|---|---|---|---|
| **Data collection and processing** | | | |
| Microscope | Titan Krios | Titan Krios | Titan Krios |
| Camera | K3 | K3 | K3 |
| Magnification | 81,000× | 81,000× | 81,000× |
| Voltage (kV) | 300 | 300 | 300 |
| Electron exposure ($e^- Å^{-2}$) | 80 | 80 | 80 |
| Automation software | EPU | EPU | EPU |
| Number of frames | 80 | 80 | 80 |
| Defocus range (μm) | −0.5 to −2.5 | −0.5 to −2.5 | −0.5 to −2.5 |
| Pixel size (Å) | 1.06 | 1.06 | 1.06 |
| Symmetry imposed | *C1* | *C1* | *C1* |
| Number of micrographs | 9453 | 9453 | 9453 |
| Initial particle images (no.) | 1.04M | 1.04M | 1.04M |
| Final particle images (no.) | 51,488 | 103,272 | 57,506 |
| Map resolution (Å) at 0.143 FSC threshold | 3.6 (global) | 3.3 (global) | 3.5 (global) |
| | 3.1 (CI-PA) 3.3 (CI-MA) | 2.9 (CI-PA) 3.2 (CI-MA) | 3.1 (CI-PA) 3.3 (CI-MA) |
| | 3.2 ($CIII_2$) | 3.1 ($CIII_2$) | 3.2 ($CIII_2$) |
| | 3.4 (C-CIV) 3.8 (S-CIV) | 3.3 (CIV) | 3.8 (CIV) |
| **Refinement** | | | |
| Initial model used (PDB code) | 6g2j/7o3c | 6g2j/7o3c | 6g2j/7o3c |
| Refinement package | Phenix, real space | Phenix, real space | Phenix, real space |
| Model resolution (Å) at 0.5 FSC threshold | 3.2 | 3.2 | 3.2 |
| Local resolution range (Å) | 3.1–19.1 (global) | 3.0–12.0 (global) | 3.0–15.4 (global) |
| | 2.9–11.7 (CI-PA) | 2.8–5.9 (CI-PA) | 2.9–7.0 (CI-PA) |
| | 3.1–7.4 (CI-MA) | 3.0–6.5 (CI-MA) | 3.0–8.2 (CI-MA) |
| | 3.1–8.8 ($CIII_2$) | 3.0–7.6 ($CIII_2$) | 3.1–9.6 ($CIII_2$) |
| | 3.6–22.0 (C-CIV) | 3.3–19.6 (CIV) | 3.6–7.1 (CIV) |
| | 3.6–7.3 (S-CIV) | | |
| Cross-correlation | | | |
| Mask | 0.84 | 0.87 | 0.85 |
| Volume | 0.84 | 0.87 | 0.85 |
| Map sharpening *B* factor ($Å^2$) | −47 (global)<br>−30 (CI-PA) −41 (CI-MA)<br>−26 ($CIII_2$)<br>−39 (C-CIV) −77 (S-CIV) | −42 (global)<br>−20 (CI-PA) −38 (CI-MA)<br>−41 ($CIII_2$)<br>−37 (CIV) | −41 (global)<br>−23 (CI-PA) −46 (CI-MA)<br>−42 ($CIII_2$)<br>−90 (CIV) |
| Model composition | | | |
| Nonhydrogen atoms | 130,520 | 115,643 | 115,617 |
| Protein residues | 15,934 | 14,146 | 14,151 |
| Ligands | 112 | 94 | 93 |
| *B* factors ($Å^2$) | | | |
| Protein | 115.12 | 82.95 | 108.84 |
| Ligand | 145.69 | 115.38 | 139.13 |
| Root mean square deviations | | | |
| Bond lengths (Å) | 0.004 | 0.005 | 0.005 |
| Bond angles (°) | 0.929 | 0.870 | 0.921 |
| **Validation** | | | |
| MolProbity score | 1.64 | 1.61 | 1.67 |
| EMRinger score | 2.05 | 2.78 | 2.29 |

**Table 1 (continued) | Cryo-EM collection, maps and model statistics of the SCs**

| | #1 CS-respirasome $CIC_2III_2IV_2$ (PDB 8PW5) | #2 C-respirasome $CIC_2III_2IV$ (PDB 8PW6) | #3 A-respirasome $CIC_2III_2IV$ (PDB 8PW7) |
|---|---|---|---|
| Clashscore | 7.27 | 6.62 | 7.64 |
| Poor rotamers (%) | 0.04 | 0.02 | 0.07 |
| Cβ deviations (%) | 0.01 | 0.00 | 0.01 |
| CaBLAM outliers (%) | 1.73 | 1.69 | 1.74 |
| Ramachandran plot | | | |
| Favored (%) | 96.38 | 96.34 | 96.26 |
| Allowed (%) | 3.61 | 3.66 | 3.73 |
| Disallowed (%) | 0.01 | 0.01 | 0.01 |

FSC, Fourier shell correlation.

be fully purified biochemically (Extended Data Fig. 1), our previous work has shown[6] that the separation of oxidative phosphorylation SCs can be achieved by three-dimensional (3D) classification during the cryo-EM data processing (Extended Data Figs. 3 and 4). One major species emerging from cryo-EM analyses of liver SCs was, as expected, $CIC_2III_2$, while CIV-containing species revealed three different architectures (at 3.3–3.6 Å overall and up to 2.9 Å focused refinement resolution), representing roughly similar amounts of particles. One of them was the 'canonical' respirasome, structurally characterized by multiple labs from various mammalian species and tissues[2–4,7,8,34,35], that is the C-respirasome or $CIC_2III_2IV$ (Fig. 1d) where CIV contains COX7A (specifically COX7A2 in brain and liver). Additionally, we determined the structures of two previously unresolved respirasomes. One of them represents the aforementioned, but so far structurally undefined, S-respirasome, a SC containing SCAF1 (Fig. 1b). It features an additional copy of CIV, joined by SCAF1 to $CIII_2$ and located next to the canonical CIV. We propose to term this $CIC_2III_2IV_2$ the CS-respirasome to reflect the presence of two copies of CIV, one with COX7A and one with SCAF1. Another novel respirasome that we identified has one COX7A-containing copy of CIV located at the back of CI (Fig. 1c) instead of at the tip of the membrane arm (Fig. 1d). We propose to term this $CIC_2III_2IV$ the A-respirasome (for alternative respirasome).

The same three (C-, CS- and A-) respirasome species, alongside $CIC_2III_2$, were identified in the brain sample (Extended Data Fig. 4). Although the number of particles, thus the overall resolution (3.9–4.0 Å), were lower than with the liver sample, each of the three respirasomes could be unambiguously identified by cryo-EM density features. Having consistently observed the three main HMW SC bands (CS-respirasome, A/C-respirasome and $CIC_2III_2$) in BN-PAGE of mouse liver, brain, kidney, heart and ovine heart, corresponding to conserved structural features between mouse liver and brain, we hypothesize that CS- and A-respirasomes are a common feature of mammalian tissues, along with the canonical C-respirasome and $CIC_2III_2$, observed in several mammalian species/tissues (for example, ovine/bovine/porcine/murine heart and human kidney)[2–5,7,8,35]. Below we use the liver maps and models to describe the structural features of the SCs, unless stated otherwise.

The CS- and A-respirasomes were not identified alongside the C-respirasome by previous single-particle cryo-EM analyses[2,3,7,8]. Nevertheless, some of the in situ tomography reconstructions of bovine heart respirasomes showed a partial density corresponding to the additional CIV in the CS-respirasome[35]. Also, both the CS- and the A-respirasome are in principle compatible with the reported in situ arrangement of CI, $CIII_2$ and CIV in rat mitochondria[36] if neighboring SCs are considered. Since our structures are consistently found in mouse liver and brain, coming from independent preparations, and are compatible with the in situ data, we suggest that the C-, CS- and A-respirasomes probably represent native SCs, despite being derived from solubilized material. Future in situ tomography studies of intact mitochondria should confirm the identity and composition of SCs directly in the organelle.

## SCAF1 is a subunit of the CS-respirasome

The structures obtained from mouse livers were of high enough resolution to reliably refine atomic models of each complex for the three respirasomes (Extended Data Figs. 3 and 5, and Extended Data Table 1). This proved that, while both the A- and the C-respirasome feature COX7A2 (the ubiquitously expressed COX7A isoform), the CS-respirasome contains COX7A2 in the CIV monomer found in the 'canonical' position, but features SCAF1 in the additional CIV monomer (Fig. 1b,d). Figure 2 shows how the density analysis guided the isoform assignment. We previously demonstrated that in SC $CIII_2IV$ the N terminus of SCAF1 binds within the mitochondrial processing peptidase (MPP) cavity of $CIII_2$ while the C terminus takes the position of COX7A in CIV[6]. Accordingly, the $CIII_2$ map in the CS-respirasome shows the N-terminal density of SCAF1 bound to $CIII_2$ (Fig. 2b, left), while no corresponding density was found in the A- and C-respirasomes (Fig. 2b, middle and right). Consistently, as judged by the different pattern of COX7A bulky side chains (Fig. 2c), the additional CIV ($CIV_S$) in the CS-respirasome features SCAF1 (Fig. 2c, left), while the canonical CIV ($CIV_C$), along with the only CIV in the A- and C-respirasomes, contains COX7A2 (Fig. 2c, middle and right). Although the linker region of SCAF1, between the $CIII_2$-interacting N terminus and the CIV-interacting C terminus is disordered, the distance between the resolved regions is compatible with the linker length, suggesting that $CIII_2$ and the $CIV_S$ of the CS-respirasome are connected by the linker[32,33].

Our data clarify why SCAF1 was considered by some to be part of the respirasome, although respirasome structures feature COX7A in CIV and no SCAF1 density in $CIII_2$[6,31]. We show that SCAF1, observed earlier by western blotting and mass spectrometry in the HMW area, is associated exclusively with the novel CS-respirasome of higher molecular weight than the canonical C-respirasome (due to the second CIV copy). From the three major HMW bands (Fig. 1a and Extended Data Fig. 2), the top represents the CS-respirasome and the bottom $CIC_2III_2$. The A- and C-respirasomes are of similar molecular weight, thus probably overlap on BN-PAGE, representing the middle band. It is now also clear why the CS-respirasome does not exist in C57BL/6J-derived samples, where SCAF1 is not functional—the second copy of CIV cannot be attached to $CIII_2$ without the bridging SCAF1.

## Comparison with C-respirasomes and $CIII_2IV$

The overall arrangement of CI, $CIII_2$ and specifically $CIV_C$ in the mouse C- and CS-respirasomes resembles previously determined C-respirasome structures[2,3,8,35,36]. When compared to the ovine heart C-respirasome,

https://doi.org/10.1038/s41594-024-01255-0

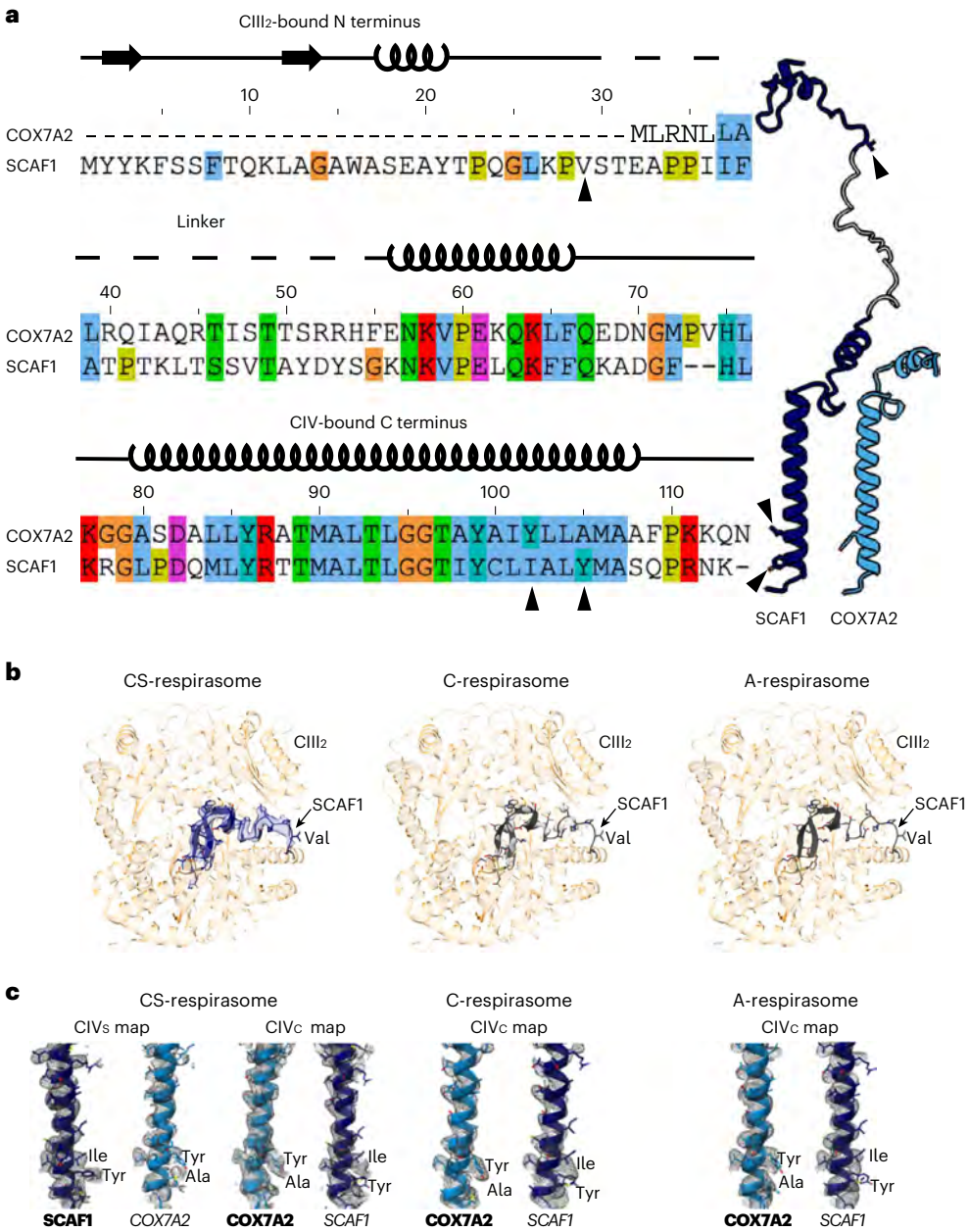


**Fig. 2 | COX7A isoforms in CIV. a**, Sequence alignment of mouse COX7A2 to SCAF1. Secondary structure sketches are depicted above the alignment and the three sections of SCAF1 are indicated: the N terminus bound to $CIII_2$ (shown in **b**), the disordered linker (depicted as a dotted line) and the C terminus bound to CIV (analyzed in **c**). The black arrowheads highlight the end of the N terminus bound to $CIII_2$ (Val29) and the position of the two bulky residues indicated in **c**. SCAF1 and COX7A2 are also shown as cartoon representation to the right of the alignment: arrowheads on SCAF1 correspond to the positions highlighted in the alignment, SCAF1 is dark blue, apart from the flexible linker in gray, COX7A2 is light blue. **b**, Model of the matrix MPP cavity of $CIII_2$, with the core subunits in orange and partially transparent and the N terminus of SCAF1, either in blue (left) or in gray (middle and right), all shown as secondary structures. The model is fitted into the cryo-EM maps of CS-, C- and A-respirasomes, as indicated above the panels and the map region corresponding to SCAF1 is shown, partially transparent, either in blue (for CS-respirasome) or in gray (for C- and A-respirasome). Only the CS-respirasome shows SCAF1 density. **c**, Density analysis of the C terminus of COX7A in the three respirasomes: each map is indicated above the models and shown in gray, with either SCAF1 (dark blue) or COX7A2 (light blue) models fitted into them. The fitted model is indicated at the bottom of each panel and the bulky side chains that allow to discriminate the subunit are indicated next to their position in the models. For each map, the model corresponding to the correct isoform is shown on the left, with the subunit name highlighted in bold.

for which a tight and a loose conformation were described differing in the CIV orientation, our structures show an intermediate conformation closer to the loose, both for the C-respirasome and for the CS-respirasome (Extended Data Fig. 6a,b). As a result, the $CIV_C$ in the mouse C-respirasome is shifted away from $CIII_2$, as highlighted by the circle in Extended Data Fig. 6a, encompassing helices from the tight ovine CIV but not from mouse $CIV_C$, or ovine loose CIV. This shift is required in the CS-respirasome to accommodate $CIV_S$: the tight conformation is incompatible with the CS-respirasome due to a clash between the $CIV_C$ and $CIV_S$, involving the portion of CIV encircled in the top of Extended Data Fig. 6b. Since our purification strategy for mouse material is substantially faster than the one used for the ovine respirasomes[3] (mitochondria fully isolated within 2 h postmortem, versus at least 6 h for the ovine procedure, and EM grids frozen within

https://doi.org/10.1038/s41594-024-01255-0

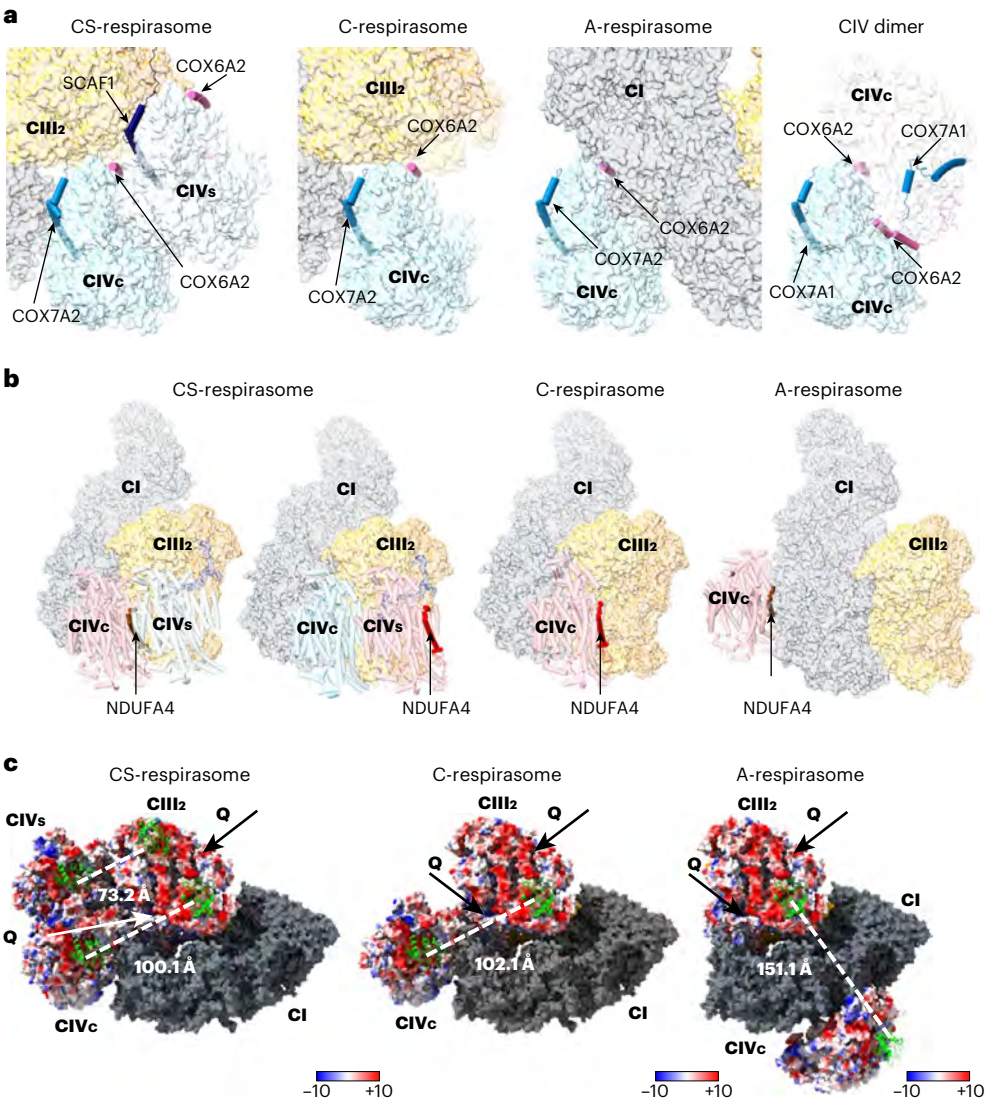


**Fig. 3 | Interfaces of CIV and position of electron carriers. a**, Surface representation of the SCs, plus the crystal structure of CIV dimer from bovine mitochondria (PDB 1occ), with the complexes colored as in Fig. 1 and rendered partially transparent, except for the highlighted chains (COX6A2 hot pink, SCAF1 dark blue and COX7A2 light blue), all shown as secondary structures with piped helices. **b**, Overlay of the SCs, represented as in **a**, to CIV from PDB 5z62 (in salmon, with piped helices) superimposed to the different positions of CIV in each panel. The NDUFA4 subunit, with location derived from PDB 5z62 as it is not identified in our maps, is highlighted in red when exposed to the membrane ($CIV_S$ of CS-respirasome or $CIV_C$ of C-respirasome), or in brown when buried (with clashes) at an interface ($CIV_C$ of CS-respirasome or A-respirasome). **c**, The arrangement of cyt *c* binding sites in SCs. Cyt *c* (green) docked on $CIII_2$ and CIV (colored as surface charge, calculated on the basis of coulombic potential in ChimeraX) based on PDBs 3cx5 (CIII-bound cyt *c*) and 5iy5 (CIV-bound cyt *c*), respectively, in all the possible binding sites of CS-, C- and A-respirasomes. The distances between the Fe atoms of the closest sites between $CIII_2$ and CIV are indicated as white dotted lines and measured in Å. The access to the quinone (Q) binding sites on $CIII_2$ is indicated as arrows. In SC respirasome one of the arrows is white. CI is in gray.

10 h after solubilization, versus at least 20 h) and the tight respirasome is incompatible with the CS-respirasome, it appears that the loose conformation represents a native state of the SC and is not a byproduct that accumulates over time, as previously reported[3]. The mainly tight ovine heart respirasome was observed in digitonin-purified sample[3] and a major class of bovine heart sample prepared in amphipols[8] also corresponded to the tight conformation[37]. Therefore, the amphipol purification used in this work does not per se result in loss of the tight conformation and the loose respirasome is indeed not an artifact. It rather appears that these two conformations represent the predominant state in different tissues: in addition to the aforementioned bovine heart structure, the position of CIV in the structure of porcine heart C-respirasome (Protein Data Bank (PDB) 5gup)[4] resembles that in ovine tight respirasome, while that in human kidney cells (PDB 5xth)[7] is similar to ovine loose. It is thus likely that in different tissues the position of CIV in the C-respirasomes varies between predominantly tight (heart) and loose (liver/brain/kidney).

Since $CIII_2$ and $CIV_S$ in the CS-respirasome are joined by SCAF1 similarly to $CIII_2CIV$[6], we can compare their relative orientation by aligning the structures on $CIII_2$ using SCAF1-containing monomer (Extended Data Fig. 6c). This highlights that $CIV_S$ (held close to $CIII_2$ by SCAF1) swings away from its positions in either the 'unlocked' or 'locked' $CIII_2CIV$[6], and is stabilized in the new position within the CS-respirasome by interactions with $CIV_C$. Unlike the 'locked' $CIII_2CIV$ (inactive assembly intermediate of $CIII_2CIV$[6]), the cytochrome *c* (cyt *c*) binding site on $CIV_S$ does not clash with $CIII_2$ (Extended Data Fig. 6e, right), so both CIV copies in the CS-respirasome are in principle able to receive electrons from cyt *c* to reduce oxygen and pump protons.

### CIV interaction interfaces and features

The position of $CIV_C$ close to the 'loose' state of respirasome[3] is consistent with COX7A2 being the main subunit involved in CI-to-$CIV_C$ interaction, both in the CS- and in the C-respirasome (Fig. 3a). The main contact (COX7A2 Arg33 with ND5 Glu503, Extended Data Fig. 7a, inset 1) is conserved between CS- and C-respirasome[3]. The COX7A2 homolog SCAF1 is involved in the interaction between $CIII_2$, $CIV_S$ and $CIV_C$ of the CS-respirasome. This interface also features COX6A2 of $CIV_C$, which appears to be a consistent interaction partner for CIV across multiple SCs. COX6A2 interacts with $CIII_2$ both in the CS- and C-respirasome (Fig. 3a). Additionally, it participates in the interaction with CI in the A-respirasome, with CIV itself in the CIV dimer and with $CIII_2$ in the 'unlocked' state of $CIII_2CIV$[6].

Within the CS-respirasome, $CIV_S$ and $CIII_2$ mostly interact at the matrix side of the membrane, where they are tethered via SCAF1: the CIV-bound N terminus of SCAF1 transmembrane (TM) helix strongly interacts with the N terminus of $CIII_2$ UQCR11, including a hydrogen bond between Gln83 and Arg11 (Extended Data Fig. 7a, inset 2). A cardiolipin molecule (negatively charged) placed here between SCAF1 ($CIV_S$), UQCR11 ($CIII_2$) and COX6A2 ($CIV_C$) joins all three complexes via bonds to three arginines from these subunits (Extended Data Fig. 7a, inset 2). The interface between $CIV_S$ and $CIII_2$ is further stabilized by the N-terminal helix of UQCRB ($CIII_2$), extending toward $CIV_S$ and forming several hydrogen bonds with COX3 residues, including Asn157 and Gln161 (Extended Data Fig. 7a, inset 3). The interface between the two copies of CIV is quite tight and is stabilized on the intermembrane space side by a phosphatidylcholine molecule (Extended Data Fig. 7a, inset 2) and a contact between Ser101 (COX4 $CIV_S$) and Asp300 (COX1 $CIV_C$) (Extended Data Fig. 7a, inset 4). On the matrix side Ser11 (COX8B $CIV_S$) interacts with Tyr179 (COX1 $CIV_C$) (Extended Data Fig. 7a, inset 4). Overall, due to many additional contacts both copies of CIV are clearly better stabilized within the CS-respirasome than a single CIV within the C-respirasome, possibly improving the stability of CS-respirasomes in situ.

In the A-respirasome, at the matrix side COX6A2 (CIV) interacts with the N terminus of NDUFA10 (CI) so that Asn14 is hydrogen bonded to the backbone oxygen of Leu10 (Extended Data Fig. 7b, inset 1). In the membrane, most of NDUFC1 TM helix (CI) interacts with COX3 (CIV), including a close contact between Gln33 and Trp259 (Extended Data Fig. 7b, inset 2). At the matrix side, the N terminus of NDUFB1 extends out of CI and abuts COX1 of CIV (Extended Data Fig. 7b, inset 3). Furthermore, in the A-respirasome, subunits COX3 and COX6A2 partially enclose a void in the membrane side of CI (Extended Data Fig. 7b, inset 4) left by the absence of TM helices 1–3 in mammalian ND2 (ref. 38). These helices are highly conserved in other species, but surprisingly their absence in higher metazoans is not compensated by supernumerary subunits. The role of ND2 truncation is thus unclear. In the A-respirasome it creates a cavity between CI and CIV, where CIV interacts with CI dGTP-containing subunit NDUFA10[39]. Speculatively, this arrangement may help regulate the activity of the A-respirasome in response to, for example, mitochondrial dNTP availability[39], if the conformation of NDUFA10 (and possibly its interaction with CIV) changes in the absence of dGTP.

We observed that the recently established CIV subunit NDUFA4, resolved from the structure of the human C-respirasome[31], and featured as a weak (not modeled) density in the ovine respirasome[40], was not resolved in any of our structures. In particular (Fig. 3b), when the human CIV is overlaid to the $CIV_C$ of CS-respirasome, or to the CIV of the A-respirasome, NDUFA4 clashes/overlaps with the $CIV_S$ or CI, respectively, indicating that this subunit cannot be attached to CIV in these positions. Conversely, in the $CIV_S$ of the CS-respirasome and in the C-respirasome, NDUFA4 would face the lipid membrane, but no corresponding density was observed. It is possible that, since the subunit is probably loosely attached to the SC, given its relatively weak density in the human[31] and ovine C-respirasomes[40], it might be lost during the exchange from digitonin to amphipol. Therefore, it is possible that NDUFA4 binds CIV substoichiometrically, being incorporated in SCs only when the corresponding position is exposed and does not clash with other complexes. Alternatively, binding of NDUFA4 may regulate to which SC (if any) a newly synthesized CIV could be assembled. Further investigation is required to fully clarify the role of NDUFA4.

### Complex I conformation

High resolution and map quality (Extended Data Fig. 8c–e) allowed us to refine near-complete atomic models of mouse CI (Table 2), featuring a dGTP molecule in NDUFA10 (Extended Data Figs. 5a and 8f,g), in agreement with biochemical data[39], and a full set of cofactors along with many bound lipids, including those at interfaces with $CIII_2$ and CIV.

CI can exist in two main conformational states, open (with enlarged and disrupted Q cavity) and closed (with tightly enclosed Q cavity)[41]. For some species, such as *Escherichia coli*, the two states are observed only during catalytic turnover[42], while for others, such as ovine[43] or *Chaetomium thermophilum*[44], both can be observed also in apo 'as purified' samples. In our universal model of CI mechanism[42], the enzyme cycles between the two states during the catalytic cycle, while in the alternative interpretation the closed state is considered 'active' and all open-like states are deemed 'deactive'[45]. Ovine 'as purified' CI is mostly in the open state—10–30% closed for isolated CI[42,43] and about 30% closed in $CICIII_2$[5]. In our model, the proportion of catalytically competent open state increases with extended purification of ovine CI but reaching a true deactive state (a defined extreme case of open state) requires high temperature treatment[43]. Mouse samples can be purified, as noted above, much quicker than ovine/bovine and 'as purified' mouse heart CI was previously reported to be at least 94% closed (or 'active')[46]. In our structures of mouse respirasomes CI overall appears in the closed state, according to the density features (Extended Data Fig. 5a) and the orientation of peripheral arm relative to membrane arm (Extended Data Fig. 6a). To precisely analyze CI conformation in our samples and identify any potential open state subset of particles (which would be undetected in a pool of mainly closed state particles, due to averaging during processing), we performed focus reverse classification (FRC)[5] on all CI-containing particles of the liver (and separately brain) datasets (Extended Data Fig. 8a,b), pooling the three SCs, but also the $CICIII_2$ particles, otherwise not analyzed. This resulted in 66% closed state CI in liver and 64% closed state CI in brain, confirming that apo CI is mainly in closed state across multiple mouse tissues, in the brain and liver (Extended Data Fig. 8), and also in the heart[46,47]. Still, in our samples about 35% of particles were found in the open state, even though we isolated mitochondria and purified samples at least as quickly and in a milder detergent (digitonin instead of *n*-dodecyl-β-D-maltoside) than previous mouse heart preparation[46,47]. To verify whether our samples contain any deactive CI, we assayed the NADH:quinone oxidoreduction (Extended Data Fig. 8h,i): 'as purified' CI is fully active (no delay in initial activity) but can be deactivated by treatment at 37 °C, resulting in delay of activity and slower turnover[41]. Therefore, even though the proportion of the open state is indeed lower in our mouse preparations than it is in the ovine counterpart (probably due to the freshness of the material), our observation of a substantial proportion of open state CI in mouse liver and brain samples is in line with our definition of open state of CI as catalytically competent.

In the closed states of both liver and brain datasets we observe a clear density for bound native ubiquinone (Extended Data Fig. 8f,g). The entire tail of UQ10 (copurified with the SCs) is visible within the quinone-binding cavity, in a similar conformation to that in porcine respirasome[48]. The headgroup density (in the deep Q site near cluster N2) is weaker than the tail, in contrast to our mammalian or bacterial complex I data under turnover[42,43], where the headgroup is well ordered. It is possible that under reducing (turnover) conditions Q headgroup forms stronger interactions with neighboring residues.

https://doi.org/10.1038/s41594-024-01255-0

**Table 2 | Cryo-EM collection, maps and model statistics of complex I**

| | #4 complex I Closed liver (PDB 8RGR) | #5 complex I Open liver (PDB 8RGQ) | #6 complex I Closed brain (PDB 8RGP) | #7 complex I Open brain (PDB 8RGT) |
|---|---|---|---|---|
| **Data collection and processing** | | | | |
| Microscope | Titan Krios | Titan Krios | Titan Krios | Titan Krios |
| Camera | K3 | K3 | K3 | K3 |
| Magnification | 81,000× | 81,000× | 81,000× | 81,000× |
| Voltage (kV) | 300 | 300 | 300 | 300 |
| Electron exposure ($e^{-}$ Å$^{-2}$) | 80 | 80 | 80 | 80 |
| Automation software | EPU | EPU | EPU | EPU |
| Number of frames | 80 | 80 | 80 | 80 |
| Defocus range (μm) | −0.5 to −2.5 | −0.5 to −2.5 | −0.5 to −2.5 | −0.5 to −2.5 |
| Pixel size (Å) | 1.06 | 1.06 | 1.06 | 1.06 |
| Symmetry imposed | *C*1 | *C*1 | *C*1 | *C*1 |
| Number of micrographs | 9,453 | 9,453 | 10,416 | 10,416 |
| Initial particle images (no.) | 1.04M | 1.04M | 159602 | 159602 |
| Final particle images (no.) | 604,185 | 317,317 | 95,155 | 54,486 |
| Map resolution (Å) at 0.143 FSC threshold | 3.0 (global) | 3.1 (global) | 3.2 (global) | 3.5 (global) |
| | 2.7 (CI-PA) | 2.8 (CI-PA) | 2.7 (CI-PA) | 2.9 (CI-PA) |
| | 2.9 (CI-MA) | 3.0 (CI-MA) | 3.0 (CI-MA) | 3.1 (CI-MA) |
| **Refinement** | | | | |
| Initial model used (PDB code) | 6g2j | 6g2j | 6g2j | 6g2j |
| Refinement package | Phenix, real space | Phenix, real space | Phenix, real space | Phenix, real space |
| Model resolution (Å) at 0.5 FSC threshold | 2.8 | 3.0 | 3.0 | 3.1 |
| Local resolution range (Å) | 2.6–4.3 (CI-PA) | 2.7–4.7 (CI-PA) | 2.5–4.9 (CI-PA) | 2.7–5.7 (CI-PA) |
| | 2.7–5.4 (CI-MA) | 2.8–6.2 (CI-MA) | 2.7–7.8 (CI-MA) | 2.9–8.8 (CI-MA) |
| Cross-correlation | | | | |
| Mask | 0.91 | 0.90 | 0.91 | 0.90 |
| Volume | 0.91 | 0.90 | 0.91 | 0.90 |
| Map sharpening *B* factor (Å$^2$) | −59 (global) | −66 (global) | −18 (global) | −21 (global) |
| | −58 (CI-PA) | −63 (CI-PA) | −25 (CI-PA) | −27 (CI-PA) |
| | −71 (CI-MA) | −65 (CI-MA) | −28 (CI-MA) | −31 (CI-MA) |
| Model composition | | | | |
| Nonhydrogen atoms | 68,141 | 67,118 | 67,868 | 67,123 |
| Protein residues | 8,236 | 8,151 | 8,222 | 8,151 |
| Ligands | 49 | 43 | 45 | 43 |
| *B* factors (Å$^2$) | | | | |
| Protein | 97.77 | 105.07 | 85.16 | 92.97 |
| Ligand | 144.32 | 144.90 | 125.98 | 132.65 |
| Root mean square deviations | | | | |
| Bond lengths (Å) | 0.005 | 0.004 | 0.006 | 0.005 |
| Bond angles (°) | 0.687 | 0.792 | 0.748 | 0.811 |
| **Validation** | | | | |
| MolProbity score | 1.67 | 1.61 | 2.06 | 1.51 |
| EMRinger score | 3.83 | 3.07 | 3.48 | 2.88 |
| Clashscore | 5.28 | 6.53 | 5.92 | 6.09 |
| Poor rotamers (%) | 1.62 | 0.01 | | 0.00 |
| Cβ deviations (%) | 0.00 | 0.00 | 0.00 | 0.00 |
| CaBLAM outliers (%) | 1.74 | 1.81 | 3.14 | 1.80 |
| Ramachandran plot | | | | |
| Favored (%) | 96.51 | 96.28 | 93.97 | 96.16 |
| Allowed (%) | 3.48 | 3.71 | 6.03 | 3.82 |
| Disallowed (%) | 0.01 | 0.01 | 0.00 | 0.01 |

The quinone density is absent in open states, consistent with previous data[42,43].

A feature of CI in the brain is the presence of a long version of subunit NDUFV3 (refs. 49,50) (Extended Data Fig. 4e,f), present in this tissue alongside the ubiquitously expressed short version[50]. In agreement with previous findings[50], we observed a strong band corresponding to the long version of NDUFV3 in our preparations of SCs from the mouse brain (Extended Data Fig. 4f). Thus, if the additional 360-residue N-terminal extension of the long isoform was ordered, it should have been possible to identify it in 3D classification of cryo-EM data. However, we were not able to detect any structured density corresponding to the N terminus of NDUFV3 in any class, probably because this region is unstructured in the context of the complex, as predicted by AlphaFold (Extended Data Fig. 4e). The role of the NDUFV3 extension in the brain may thus lie in the transient regulatory interactions with yet unknown protein partners[51].

## Functional implications

Our structures add A- and CS-respirasomes to the previously observed SCs C-respirasome, $ClCIII_2$ and $CIII_2CIV$. According to our biochemical analysis (Extended Data Fig. 2), these structures clarify the composition of the BN-PAGE bands around $ClCIII_2CIV$, while additional uncharacterized species remain at higher molecular weight, potentially representing megacomplex-type assemblies, for example, as reported in human cell lines[7]. The currently available structures from human[7], ovine[3,5], mouse (Extended Data Figs. 3 and 4), porcine[2,4] and bovine[8,34,35] origin point toward the conserved arrangement of complexes in the C-respirasome and $ClCIII_2$. We thus hypothesize that the CS-respirasome, observed in BN-PAGE of human[32], zebrafish[30], ovine and mouse (Extended Data Fig. 2) samples through the presence of SCAF1 at HMW is also probably structurally conserved across vertebrates. The structural analysis of further species would test this hypothesis, particularly also for the A-respirasome, which cannot be biochemically separated from the C-respirasome given the identical composition.

Our data allow to clarify the long-standing debate on the existence of SCAF1-containing 'respirasomes', while the potential functional implications of different respirasomes remain to be established. It was suggested that the S-MRC (where MRC is the mitochondrial respiratory chain) consisting of the CS-respirasome and $CIII_2CIV$, both dependent on SCAF1, sustains the adaptation to anaerobic ATP synthesis via glycolysis and lactic fermentation, while the C-MRC, consisting of the C-respirasome and free $CIII_2$ and CIV, is more efficient in coupling respiration to ATP synthesis (for example, in muscle tissue)[32]. In vivo the two MRC types probably coexist in different ratios in different tissues, potentially depending on metabolic conditions[32]. Although the metabolic roles of the C- versus S-MRCs remain to be investigated in vivo, based on the aforementioned biochemical findings and our structures, we speculate that the CS-respirasome, containing two copies of CIV, might be adapted to operate at low oxygen concentrations, ensuring adequate electron flow downstream of $CIII_2$. This hypothesis would be in line with a potential kinetic advantage of SCs, bringing the substrate binding sites of different complexes closer than in the random diffusion model. This contrasts with the previously proposed[52,53] substrate channels, which do not exist in any SCs[3,6], including the structures reported here.

The kinetic advantage of $CIII_2CIV$ over the isolated $CIII_2$ and CIV, considered an evolutionarily conserved trait as it is observed in yeast[54] and mouse[6], was ascribed to a negative surface charge on the intermembrane space side, allowing the positively charged cyt *c* to slide along the surface from $CIII_2$ to CIV (two-dimensional (2D) diffusion), thus increasing its local concentration and promoting the SC activity[6,54]. Within the CS-respirasome, the negatively charged surface extends from $CIII_2$ over both copies of CIV (Fig. 3c) and the distances from both $CIII_2$ sites where cyt *c* is reduced to the oxidation sites on $CIV_S$ and $CIV_C$ are roughly similar (around 7 nm and 10 nm, respectively, Fig. 3c) to

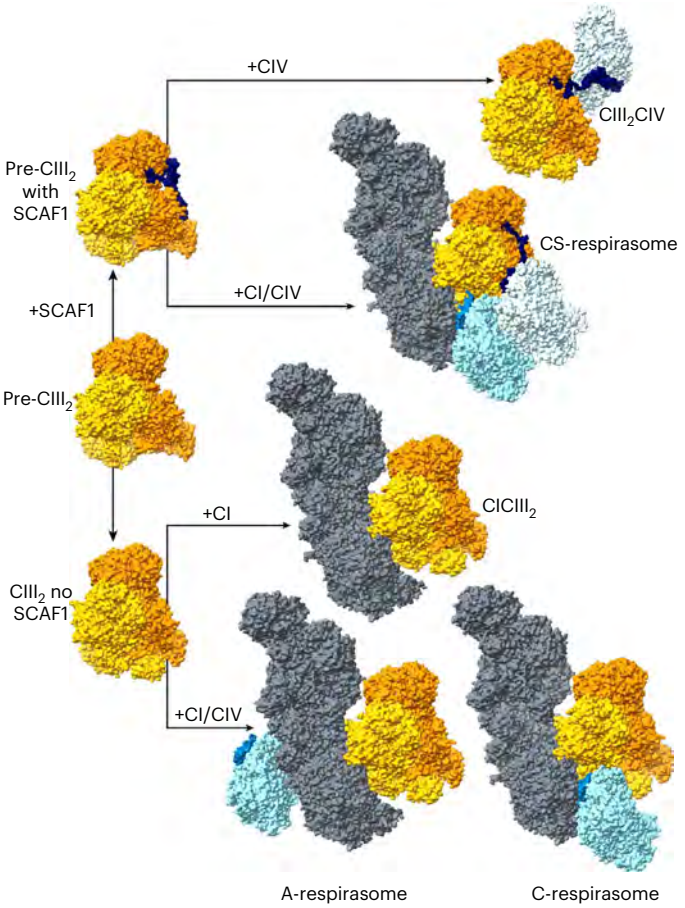


**Fig. 4 | Updated overview of the broad assembly pathways of mitochondrial SCs.** Schematic representation of the different SCs observed in the mouse mitochondrial membranes, depicted as in Figs. 1–3, adding the previously known species to the ones described in this manuscript. $CIII_2CIV$ is from PDB 7o3c, $ClCIII_2$ is fitted to the map resulting from classification of our data (in perfect agreement with previously published structures of this SC).

those in $CIII_2CIV$[6]. We hypothesize that this in principle allows for the observed kinetic advantage of $CIII_2CIV$ over individual $CIII_2$ and CIV to be conserved in the CS-respirasome, where the potentially high $CIII_2$/cyt *c* redox capacity may be sustained by two copies of CIV (in comparison to the single copy present in $CIII_2CIV$). Future activity assays performed on the currently unattainable pure and homogeneous CS-respirasome will be required to test this hypothesis.

Furthermore, it appears that the cyt *c* binding site on $CIV_S$ (modeled on PDB 5iy5) can be complemented by an additional interaction with $CIV_C$ COX6B1 (for example, Lys46 bound to cyt *c* Glu21) (Extended Data Fig. 6d). This may increase the affinity for reduced cyt *c*, potentially improving rates downstream of $CIII_2$. Finally, as noted previously[3], within the C-respirasomes one quinol binding site of $CIII_2$ is exposed, facing the quinol exit from CI and thus optimal for activity, while the opposite (distal) site in $CIII_2$ is partially obscured by $CIV_C$, introducing a possible asymmetry in the activity of the two $CIII_2$ monomers. Such asymmetry was observed in the bovine heart C-respirasome[8]: the iron–sulfur protein (ISP) domain facing CIV was resolved (thus apparently being inactive), while the other ISP was proposed to be active (being unresolved and thus mobile as needed for activity). However, later structures of $CIII_2$-containing SCs did not reveal such asymmetry[2–4,6,7], and in all SCs reported here the ISP domains have similarly weak densities, probably reflecting their inherent flexibility. This makes it hard to draw conclusions on the functional asymmetry of $CIII_2$ based on the ISP density.

In the CS-respirasome the distal Q site in $CIII_2$ is even more obscured than in the C-respirasome due to the presence of $CIV_S$ (although in principle the quinone can still access the distal site through the remaining openings) and so essentially only one monomer may be fully active within the $CIII_2$ dimer. This may lower the cyt *c* reduction rates if needed to align with low oxygen concentrations and thus low overall CIV activity.

By contrast, in the A-respirasome both Q sites in $CIII_2$ are exposed to lipid and free to accept quinol, potentially enabling efficient and fast $CIII_2$ operation. Instead, CIV is located almost as far away from $CIII_2$ as possible within the A-respirasome (15 nm between the cyt *c* sites), potentially lowering the cyt *c* oxidation rates. Furthermore, in this conformation the negatively charged surface corridor for 2D diffusion of cyt *c* between $CIII_2$ and CIV is disrupted. We speculate that this arrangement may help to adapt to high oxygen concentrations and thus high CIV activity, especially in cases when CI activity is relatively low in supplying quinol to $CIII_2$. In conditions such as aerobic glycolysis (also known as the Warburg effect) in proliferating cells, the mitochondrial NADH shuttles were found to saturate due to the high cytosolic NADH/$NAD^+$ ratio[55]. If the NADH supply to CI is limited, the reduced quinol pool may mostly come from the activity of CII and other mitochondrial quinone oxidoreductases. $CIII_2$ activity may thus vary depending on the quinol availability[55]. Under those circumstances, it might be optimal for CIV activity to be decoupled from CI/$CIII_2$ activity as in the A-respirasome (or with free CIV), where the CIV activity would depend on the 3D (rather than 2D) diffusion of cyt *c*[54] (and thus on the overall cyt *c* pool).

Brain and liver contain multiple cell types, with different exposure to oxygen and potentially in different metabolic states, not separated during our preparation. This may explain the presence of both A- and SC-respirasomes (along with C-respirasome) in our samples.

In line with the A-respirasome structure, in SCs from *Tetrahymena thermophila*[56,57] CIV binds to the same region of CI, resulting in a 17 nm distance between the two cyt *c* sites, similar to the 15 nm observed in our structure (although in *T. thermophila* CI and CIV mainly interact via supernumerary subunits absent in mammals). Another way to regulate CIV activity in the context of SCs was observed in *Mycobacterium smegmatis*, where the proton uptake by CIV is around 40 times slower within the $CIII_2CIV_2$ SC as opposed to isolated CIV because the extension of CIII subunit QcrB obstructs the proton uptake D-pathway of CIV[58].

Our results also refine the current view[6,40] on the assembly pathways of SCs. Based on the structures, SCAF1 binding to the $CIII_2$ precursor (Fig. 4) appears to determine the composition of the maturing SCs: the SCAF1-bound $CIII_2$ can either join with CIV leading to $CIII_2CIV$, or with CI and two copies of CIV, resulting in the CS-respirasome. It remains to be clarified whether some assembled $CIII_2CIV$ may also be incorporated into the CS-respirasome. Conversely, if $CIII_2$ is not bound to SCAF1, it cannot form $CIII_2CIV$ or the CS-respirasome, thereby being incorporated in the remaining SCs—$CICIII_2$, the A-respirasome and the C-respirasome, the last two containing exclusively COX7A1 or COX7A2 on CIV, depending on the tissue, but no SCAF1. Overall, the structures allow us to propose a hypothesis to explain how SCAF1 expression, which can be, for example, upregulated by estrogen in tumor cells[13], might drive the adaptation of cells toward low oxygen conditions[13,32], promoting the CS-respirasome and $CIII_2CIV$ formation, while $CICIII_2$, the C-respirasome and the A-respirasome, formed without SCAF1, may be optimal for efficient respiration at normal or high oxygen concentrations. Future experiments will be necessary to test this mechanism in vivo by, for example, monitoring the metabolism of cells derived from various mammalian species under different oxygen (or proliferation) conditions, while in parallel biochemically and structurally characterizing the SCs in each sample.

## Online content

Any methods, additional references, Nature Portfolio reporting summaries, source data, extended data, supplementary information, acknowledgements, peer review information; details of author contributions and competing interests; and statements of data and code availability are available at https://doi.org/10.1038/s41594-024-01255-0.

## References


1. Schägger, H. & Pfeiffer, K. Supercomplexes in the respiratory chains of yeast and mammalian mitochondria. *EMBO J.* **19**, 1777–1783 (2000).
2. Gu, J. et al. The architecture of the mammalian respirasome. *Nature* **537**, 639–643 (2016).
3. Letts, J. A., Fiedorczuk, K. & Sazanov, L. A. The architecture of respiratory supercomplexes. *Nature* **537**, 644–648 (2016).
4. Wu, M., Gu, J., Guo, R., Huang, Y. & Yang, M. Structure of mammalian respiratory supercomplex $I_1III_2IV_1$. *Cell* **167**, 1598–1609.e10 (2016).
5. Letts, J. A., Fiedorczuk, K., Degliesposti, G., Skehel, M. & Sazanov, L. A. Structures of respiratory supercomplex I+$III_2$ reveal functional and conformational crosstalk. *Mol. Cell* **75**, 1131–1146.e6 (2019).
6. Vercellino, I. & Sazanov, L. A. Structure and assembly of the mammalian mitochondrial supercomplex $CIII_2CIV$. *Nature* **598**, 364–367 (2021).
7. Guo, R., Zong, S., Wu, M., Gu, J. & Yang, M. Architecture of human mitochondrial respiratory megacomplex $I_2III_2IV_2$. *Cell* **170**, 1247–1257 (2017).
8. Sousa, J. S., Mills, D. J., Vonck, J. & Kühlbrandt, W. Functional asymmetry and electron flow in the bovine respirasome. *eLife* **5**, e21290 (2016).
9. Protasoni, M. et al. Respiratory supercomplexes act as a platform for complex III-mediated maturation of human mitochondrial complexes I and IV. *EMBO J.* **39**, e102817 (2020).
10. Lobo-Jarne, T. et al. Multiple pathways coordinate assembly of human mitochondrial complex IV and stabilization of respiratory supercomplexes. *EMBO J.* **39**, e103912 (2020).
11. Diaz, F., Fukui, H., Garcia, S. & Moraes, C. T. Cytochrome c oxidase is required for the assembly/stability of respiratory complex I in mouse fibroblasts. *Mol. Cell. Biol.* **26**, 4872–4881 (2006).
12. Schägger, H. et al. Significance of respirasomes for the assembly/stability of human respiratory chain complex I. *J. Biol. Chem.* **279**, 36349–36353 (2004).
13. Ikeda, K. et al. Mitochondrial supercomplex assembly promotes breast and endometrial tumorigenesis by metabolic alterations and enhanced hypoxia tolerance. *Nat. Commun.* **10**, 1–15 (2019).
14. Wang, G., Popovic, B., Tao, J. & Jiang, A. Overexpression of COX7RP promotes tumor growth and metastasis by inducing ROS production in hepatocellular carcinoma cells. *Am. J. Cancer Res* **10**, 1366–1383 (2020).
15. Hollinshead, K. E. R. et al. Respiratory supercomplexes promote mitochondrial efficiency and growth in severely hypoxic pancreatic cancer. *Cell Rep.* **33**, 108231 (2020).
16. Rohlenova, K. et al. Selective disruption of respiratory supercomplexes as a new strategy to suppress $Her2^{high}$ breast cancer. *Antioxid. Redox Signal* **26**, 84–103 (2017).
17. Antoun, G. et al. Impaired mitochondrial oxidative phosphorylation and supercomplex assembly in rectus abdominis muscle of diabetic obese individuals. *Diabetologia* **58**, 2861–2866 (2015).
18. Huertas, J. R., Al Fazazi, S., Hidalgo-Gutierrez, A., López, L. C. & Casuso, R. A. Antioxidant effect of exercise: exploring the role of the mitochondrial complex I superassembly. *Redox Biol.* **13**, 477–481 (2017).
19. Greggio, C. et al. Enhanced respiratory chain supercomplex formation in response to exercise in human skeletal muscle. *Cell Metab.* **25**, 301–311 (2017).
20. Gonzalez-Franquesa, A. et al. Mass-spectrometry-based proteomics reveals mitochondrial supercomplexome plasticity. *Cell Rep.* **35**, 109180 (2021).

21. Granata, C. et al. High-intensity training induces non-stoichiometric changes in the mitochondrial proteome of human skeletal muscle without reorganisation of respiratory chain content. *Nat. Commun.* **12**, 7056 (2021).
22. Frenzel, M., Rommelspacher, H., Sugawa, M. D. & Dencher, N. A. Ageing alters the supramolecular architecture of OxPhos complexes in rat brain cortex. *Exp. Gerontol.* **45**, 563–572 (2010).
23. Gómez, L. A., Monette, J. S., Chavez, J. D., Maier, C. S. & Hagen, T. M. Supercomplexes of the mitochondrial electron transport chain decline in the aging rat heart. *Arch. Biochem. Biophys.* **490**, 30–35 (2009).
24. Lombardi, A. et al. Defining the transcriptomic and proteomic profiles of rat ageing skeletal muscle by the use of a cDNA array, 2D- and Blue native-PAGE approach. *J. Proteom.* **72**, 708–721 (2009).
25. Lopez-Fabuel, I. et al. Complex I assembly into supercomplexes determines differential mitochondrial ROS production in neurons and astrocytes. *Proc. Natl Acad. Sci. USA* **113**, 13063–13068 (2016).
26. Maranzana, E., Barbero, G., Falasca, A. I., Lenaz, G. & Genova, M. L. Mitochondrial respiratory supercomplex association limits production of reactive oxygen species from complex I. *Antioxid. Redox Signal* **19**, 1469–1480 (2013).
27. Cogliati, S. et al. Mechanism of super-assembly of respiratory complexes III and IV. *Nature* **539**, 579–582 (2016).
28. Fernández-Vizarra, E. et al. SILAC-based complexome profiling dissects the structural organization of the human respiratory supercomplexes in SCAFI KO cells. *Biochim. Biophys. Acta Bioenerg.* **1862**, 148414 (2021).
29. Calvo, E. et al. Functional role of respiratory supercomplexes in mice: SCAF1 relevance and segmentation of the Qpool. *Sci. Adv.* **6**, eaba7509 (2020).
30. García-Poyatos, C. et al. Scaf1 promotes respiratory supercomplexes and metabolic efficiency in zebrafish. *EMBO Rep.* **21**, e50287 (2020).
31. Zong, S. et al. Structure of the intact 14-subunit human cytochrome c oxidase. *Cell Res* **28**, 1026–1034 (2018).
32. Fernández-Vizarra, E. et al. Two independent respiratory chains adapt OXPHOS performance to glycolytic switch. *Cell Metab.* **34**, 1792–1808.e6 (2022).
33. Benegiamo, G. et al. COX7A2L genetic variants determine cardiorespiratory fitness in mice and human. *Nat. Metab.* **4**, 1336–1351 (2022).
34. Althoff, T., Mills, D. J., Popot, J.-L. & Kühlbrandt, W. Arrangement of electron transport chain components in bovine mitochondrial supercomplex $I_1III_2IV_1$. *EMBO J.* **30**, 4652–4664 (2011).
35. Davies, K. M., Blum, T. B. & Kühlbrandt, W. Conserved in situ arrangement of complex I and III2 in mitochondrial respiratory chain supercomplexes of mammals, yeast, and plants. *Proc. Natl Acad. Sci. USA* **115**, 3024–3029 (2018).
36. Nesterov, S. et al. Ordered clusters of the complete oxidative phosphorylation system in cardiac mitochondria. *Int. J. Mol. Sci.* **22**, 1–10 (2021).
37. Letts, J. A. & Sazanov, L. A. Clarifying the supercomplex: the higher-order organization of the mitochondrial electron transport chain. *Nat. Struct. Mol. Biol.* **24**, 800–808 (2017).
38. Birrell, J. A. & Hirst, J. Truncation of subunit ND2 disrupts the threefold symmetry of the antiporter-like subunits in complex I from higher metazoans. *FEBS Lett.* **584**, 4247–4252 (2010).
39. Molina-Granada, D. et al. Most mitochondrial dGTP is tightly bound to respiratory complex I through the NDUFA10 subunit. *Commun. Biol.* **5**, 620 (2022).
40. Vercellino, I. & Sazanov, L. A. The assembly, regulation and function of the mitochondrial respiratory chain. *Nat. Rev. Mol. Cell Biol.* **23**, 141–161 (2021).
41. Sazanov, L. A. From the 'black box' to 'domino effect' mechanism: what have we learned from the structures of respiratory complex I. *Biochem. J.* **480**, 319–333 (2023).
42. Kravchuk, V. et al. A universal coupling mechanism of respiratory complex I. *Nature* **609**, 808–814 (2022).
43. Kampjut, D. & Sazanov, L. A. The coupling mechanism of mammalian respiratory complex I. *Science* **370**, eabc4209 (2020).
44. Laube, E., Meier-Credo, J., Langer, J. D. & Kühlbrandt, W. Conformational changes in mitochondrial complex I of the thermophilic eukaryote *Chaetomium thermophilum*. *Sci. Adv.* **8**, 9952 (2022).
45. Chung, I. et al. Cryo-EM structures define ubiquinone-10 binding to mitochondrial complex I and conformational transitions accompanying Q-site occupancy. *Nat. Commun.* **13**, 1–13 (2022).
46. Agip, A. N. A. et al. Cryo-EM structures of complex I from mouse heart mitochondria in two biochemically defined states. *Nat. Struct. Mol. Biol.* **25**, 548–556 (2018).
47. Grba, D. N., Chung, I., Bridges, H. R., Agip, A. N. A. & Hirst, J. Investigation of hydrated channels and proton pathways in a high-resolution cryo-EM structure of mammalian complex I. *Sci. Adv.* **9**, eadi1359 (2023).
48. Gu, J., Liu, T., Guo, R., Zhang, L. & Yang, M. The coupling mechanism of mammalian mitochondrial complex I. *Nat. Struct. Mol. Biol.* **29**, 172–182 (2022).
49. Dibley, M. G., Ryan, M. T. & Stroud, D. A. A novel isoform of the human mitochondrial complex I subunit NDUFV3. *FEBS Lett.* **591**, 109–117 (2017).
50. Bridges, H. R., Mohammed, K., Harbour, M. E. & Hirst, J. Subunit NDUFV3 is present in two distinct isoforms in mammalian complex I. *Biochim. Biophys. Acta* **1858**, 197 (2017).
51. Dyson, H. J. & Wright, P. E. Intrinsically unstructured proteins and their functions. *Nat. Rev. Mol. Cell Biol.* **6**, 197–208 (2005).
52. Bianchi, C., Genova, M. L., Castelli, G. P. & Lenaz, G. The mitochondrial respiratory chain is partially organized in a supercomplex assembly: kinetic evidence using flux control analysis. *J. Biol. Chem.* **279**, 36562–36569 (2004).
53. Lapuente-Brun, E. et al. Supercomplex assembly determines electron flux in the mitochondrial electron transport chain. *Science* **340**, 1567–1570 (2013).
54. Moe, A. et al. Cryo-EM structure and kinetics reveal electron transfer by 2D diffusion of cytochrome c in the yeast III-IV respiratory supercomplex. *Proc. Natl Acad. Sci. USA* **118**, e2021157118 (2021).
55. Wang, Y. et al. Saturation of the mitochondrial NADH shuttles drives aerobic glycolysis in proliferating cells. *Mol. Cell* **82**, 3270–3283.e9 (2022).
56. Mühleip, A. et al. Structural basis of mitochondrial membrane bending by the I–II–$III_2$–$IV_2$ supercomplex. *Nature* **615**, 934–938 (2023).
57. Han, F. et al. Structures of *Tetrahymena thermophila* respiratory megacomplexes on the tubular mitochondrial cristae. *Nat. Commun.* **14**, 2542 (2023).
58. Król, S., Fedotovskaya, O., Högbom, M., Ädelroth, P. & Brzezinski, P. Electron and proton transfer in the *M. smegmatis* $III_2IV_2$ supercomplex. *Biochim. Biophys. Acta Bioenerg.* **1863**, 148585 (2022).

# Methods

## Animal care

The mice were housed at the Pre-Clinical Facility of IST Austria, approved by the Austrian Federal Ministry of Science, Research and Economy under the following license number: BMWFW-66.018/003-II/3b/2014. The mice were housed in commercially available individually ventilated cages made of polysulfon under standard laboratory conditions (room temperature 21–24 °C; relative humidity 55 ± 10%; photoperiod 12 h light:12 h dark) and supplied with standard diet and water ad libitum.

## Organ collection

Without any previous procedure, mice were killed by cervical dislocation and the organs were immediately excised and placed in individual precooled tubes on ice (one tube per organ). Mice were processed in batches of five to ten to minimize the waiting time before mitochondria isolation. The procedure is referred to as 'organ removal'. All animal treatments were performed in accordance with the Austrian 'Tierversuchs-Verordnung 2012 -TVV2012 (522. Verordnung)- Methoden zur Tötung von Tieren' (English translation 'Animal Experiments Ordinance 2012 -TVV2012 (522nd Ordinance)- Methods and killing of animals'), corresponding to the Annex IV (Methods of Killing Animals) of the European directive 2010/63/EU.

Ovine hearts were obtained from a local abbatoir; hence, no ethical approval was required.

## Mitochondria isolation

Ovine mitochondria were purified as described before[59], following procedure 3. The organs were placed on ice upon collection and transported to the lab, where they were minced at 4 °C. The minced meat was placed in a blender in 250 mM sucrose, 10 mM Tris HCl pH 7.8 at a ratio of 400 ml per 200 g, to which 3 ml of 2 M Tris was added. The material was blended for 15 s, 3 ml of Tris was added, and then the material was blended for 5 more seconds. The pH was readjusted to 7.8, and the homogenate was centrifuged for 20 min at 1,200*g*. The pH of the supernatant solution was readjusted to 7.8, and the material was centrifuged for 15 min at 26,000*g*. The pellet is washed twice by resuspension, first in 200 ml, then in 60 ml of sucrose solution (per 200 g of original material), pH adjustment to 7.8 and 15 min centrifugation at 26,000*g*. The final pellet was flash-frozen in liquid nitrogen and stored at −80 °C. Mouse mitochondria from heart and kidney were purified as described before[6]. The material was cut in small pieces on a Petri dish containing buffer A (250 mM sucrose, 10 mM Tris HCl pH 7.8 and 5 mM β-mercaptoethanol), 1.4 ml $g^{-1}$ of tissue. The minced tissue, devoid of buffer A, was then transferred to a Dounce homogenizer containing 1.6 ml buffer B (250 mM sucrose, 10 mM Tris HCl pH 7.8, 5 mM β-mercaptoethanol, 1 mM Tris succinate pH 7.8 and 0.2 mM ethylenediaminetetraacetic acid (EDTA)) per gram of tissue and 25 µl of 2 M Tris base and homogenized until no pieces of meat could be seen by naked eye. The same amount of buffer B + Tris base was then added to the homogenate, and the material was further homogenized for 30 strokes. The homogenate was transferred to a tube, the same amount of buffer B + Tris base was used to rinse the homogenizer, then added to the same tube and the material was centrifuged for 5 min at 1,000*g*. The supernatant was then spun down for 10 min at 9,000*g*, and the resulting pellet was washed by spinning down for 2 min at 15,000*g*, every time resuspending in half the volume of buffer B until 2 ml were reached. After a final centrifugation, the pellet was flash-frozen in liquid nitrogen and stored at −80 °C. Livers were subject to a similar procedure, but with two low-speed initial spins (3 min at 1,000*g*, then 3 min at 2,000*g*) instead of 5 min at 1,000*g* to increase separation from the cell debris pellet. Mouse brain mitochondria were purified as described before[60], with minor modifications. Each brain was placed in a 50 ml tube, containing 5 ml of MSE buffer (225 mM mannitol, 75 mM sucrose, 20 mM HEPES pH 7.4 and 1 mM EDTA) + 0.1% bovine serum albumin (BSA), upon collection. The collected brains were then transferred (without buffer) to a Dounce homogenizer containing 2.5 ml MSE + BSA per brain, then the solution was removed and replaced by the same amount of fresh buffer MSE + BSA and the brains were homogenized with 40 strokes. The homogenate was transferred to a tube, 10 ml of MSE + BSA was used to rinse the homogenizer, then added to the same tube and the material was centrifuged for 4 min at 5,000*g*. The supernatant was then transferred to a new tube, to which 0.02% digitonin was added drop-wise and tumbled on a wheel at 4 °C for 20 min. The sample was then centrifuged for 10 min at 10,000*g*, and the resulting pellet resuspended in 2 ml MSE per brain, then again centrifuged for 10 min at 10,000*g*. The mitochondrial pellet was flash-frozen in liquid nitrogen and stored at −80 °C.

## Membrane preparation

Mitochondrial membranes were extracted by breaking mitochondria with osmotic shock, as described before[6], using 1 ml MilliQ water and 1 ml buffer MM (20 mM HEPES pH 7.7, 50 mM NaCl, 10% glycerol, 1 mM EDTA, 2 mM dithiothreitol (DTT), 0.002% phenylmethylsulfonyl fluoride and cOmplete Ultra EDTA-free cocktail) per 100 mg mitochondria. The mitochondrial pellet was resuspended in MilliQ water and homogenized with 50 strokes in a Dounce homogenizer. Then KCl was added to a final concentration of 150 mM, and the sample was homogenized again for 50 strokes. The material was then centrifuged for 45 min at 30,000*g*, the pellet resuspended in buffer MM, spun down again for 45 min at 30,000*g* and resuspended in buffer MM. The total amount of protein in the extracted membranes was measured by Pierce BCA protein assay (Thermo Scientific, ref. 23227). The protein yield for each heart corresponded to about 1/3 of yield for brains, 1/5 for kidneys and 1/10 for livers. Material corresponding to approximately one heart (and corresponding amount from the other organs) was used for each biochemical experiment. Material corresponding to approximately two livers and six brains was used for the structural preparations. As the animals used corresponded to the surplus from the animal house, sex (mainly males) and age (ranging from 12 to 32 weeks) were mixed.

## Digitonin recrystallization

Digitonin, purchased from Carl Roth (4005.4), was recrystallized by adapting a published procedure[61]. Ten milliliters pure ethanol per gram of digitonin were used. Digitonin was solubilized in hot (75 °C) ethanol, then left at room temperature for 10 min and then cooled on ice for another 10 min to allow precipitation. The material was then centrifuged for 30 min at 7,000*g* at 4 °C, and the supernatant was discarded. The pellet was resuspended again in preheated ethanol (5 ml per initial gram of digitonin) and vacuum dried. This procedure yields around 60% of the initial weight, and the material is pure enough not to precipitate in the buffers used for purification.

## Purification of respiratory SCs

The mitochondrial membrane proteins were purified from the membranes following an established protocol[6], with minor modifications. Mitochondrial membranes were solubilized using a 6:1 digitonin-to-protein weight ratio in buffer MM (20 mM HEPES pH 7.7, 50 mM NaCl, 10% glycerol, 1 mM EDTA, 2 mM DTT, 0.002% phenylmethylsulfonyl fluoride, and cOmplete Ultra EDTA-free cocktail) for 1 h at 4 °C on a wheel. After solubilization, the material was spun down for 45 min at 30,000*g* to remove the insoluble fraction and loaded onto the MonoQ ion-exchange column. For the small-scale experiments shown in Extended Data Fig. 2, the protein material was measured again by Pierce BCA assay before loading on column, to make sure that the same amount per each sample tested in the same batch would be used (2–4 mg protein, according to the batch). The MonoQ 1 ml column was equilibrated in buffer QA (20 mM HEPES pH 7.7, 50 mM NaCl, 10% glycerol, 2 mM EDTA, 1 mM DTT and 0.2% digitonin), then after sample loading (2 ml for analytical purifications, 5 ml for preparative purifications) a linear gradient elution was performed with 0% to 50% buffer QB (20 mM HEPES pH 7.7, 1 M NaCl, 10% glycerol, 2 mM EDTA, 1 mM

DTT and 0.2% digitonin) in 20 ml (20 column volumes), to achieve a NaCl gradient from 50 mM to 500 mM. A typical elution pattern is shown in Extended Data Fig. 1a,b. For the analytical preparations, the fractions corresponding to the three peaks were collected to have 4.8 ml material per peak, and then each peak was concentrated to the same volume for each batch (0.5–1 ml final volume among the different batches). Extended Data Fig. 1 shows representative results of the analytical purifications: the procedure was repeated at least three times for each tissue in this format. The samples used for grids were exchanged into amphipol A8-35 (Anatrace, CAS no. 326856-53-5) after MonoQ, by incubation for 30 min on a wheel at 4 °C. A 1:1 amphipol to total solubilized protein weight ratio was used. The samples were then diluted in detergent-free buffer to a volume below the critical micelle concentration of digitonin to disrupt the micelles and reconcentrated using a 100 kDa cutoff concentrator (Vivaspin 15, 15 ml maximum volume) to 0.5 ml to be run on a Superose 6 increase 10/300 GL column equilibrated in SEC buffer (20 mM HEPES pH 7.7, 50 mM NaCl and 2 mM EDTA). A representative SEC profile is shown in Extended Data Fig. 1b. The eluted fractions were then concentrated as above, using a 0.5 ml concentrator (Vivaspin 500), to 15 µl to be put on grids. The final protein concentration was estimated using the proxy of 280 nm absorbance, due to the heterogeneous nature of the sample, and samples of 280 nm absorbance between 1 and 2 (roughly between 0.5 mg $ml^{-1}$ and 1 mg $ml^{-1}$) were frozen on grids. Figure 1a shows the native electrophoresis pattern of a representative liver sample (details about the gel and staining are below).

### Sodium dodecyl sulfate polyacrylamide gel electrophoresis

The brain CD1 material was run on sodium dodecyl sulfate polyacrylamide gel electrophoresis to detect the presence of long versus short isoforms of NDUFV3. The sample was loaded on Novex WedgeWell 4–20% Tris-glycine gel (XP04205BOX) and run at 150 V.

### BN-PAGE

The samples were run on 3–12% BisTris native gels (Invitrogen, BN1001BOX), for 1/3 of the gel at 150 V in dark cathode buffer (50 mM BisTris, 50 mM tricine and 0.02% Coomassie G-250), then for 2/3 of the gel at 250 V in light cathode buffer (50 mM BisTris, 50 mM tricine and 0.002% Coomassie G-250). At the end of the run, the gels were either stained with Coomassie (InstantBlue stain from Abcam, ab119211) or subject to in-gel activity or immunoblotting as described in the following sections.

### In-gel activity assays

In-gel activity for complexes I and IV was adapted from a previous publication[62]. After BN-PAGE, the gels were incubated with the staining solutions for complex I (3 mM nitrotetrazolium blue (4421.3, Carl Roth) and 150 µM NADH (124644, Millipore) in 10 ml of 5 mM Tris/HCl, pH 7.4) for 5 min and for complex IV (2.3 mM diaminobenzidine (D12384, Sigma-Aldrich) and 50 µM cyt *c* (C2037-1G, Sigma-Aldrich) dissolved in 10 ml of 50 mM sodium phosphate, pH 7.2) for 1 h. No fixing solution was used. Substituting the staining solution with water, exchanged every 10 min, and imaging the gels within 1.5 h did not lead to overstaining.

### Immunoblotting

The proteins were transferred to a polyvinylidene fluoride membrane for 45 min at 1 A constant current, subsequently blocked for 1 h at room temperature, or overnight at 4 °C in casein buffer (Sigma-Aldrich B6429-500ML) in Tris buffer saline Tween (TBST). The membrane was then decorated accordingly, using anti UQCRC2 (for $CIII_2$) 14742-1-AP from Proteintech 1:6,000, anti MT-CO1 (for CIV) 459600 from Invitrogen 1:4,000, anti-SCAF1 PA5-96994 from Invitrogen 1:1,000 and anti-NDUFV3 13430-1-AP from Proteintech 1:300 primary antibodies (incubated either 1 h at room temperature or overnight at 4 °C), followed by horseradish peroxidase-conjugated anti-rabbit IgG (ab205718, Abcam) and anti-mouse IgG (w4021, Promega) secondary antibodies, all used at 1:10,000 dilution and incubated 1 h at room temperature. All antibodies were diluted in casein buffer–TBST. The signal was detected using the ECL Prime kit (Cytiva RPN2232).

### Grid preparation

The concentrated samples, mixed with 0.2% CHAPS (final concentration) upon grid preparation to minimize the protein exposure to air–water interface, were frozen on Quantifoil 0.6/1, 300 mesh copper grids manually coated with a continuous layer of carbon approximately 1 nm thick[63]. The grids were glow-discharged for 5 s at 25 mA before freezing. Samples were prepared using a Vitrobot Mark IV, set to 4 °C, 100% humidity, 2 s blot time and 25 blot force. For each grid, 2.7 µl of sample was required.

### Data collection

The micrographs were collected on a IST Austria 300 kV Titian Krios G3i, equipped with Gatan K3 BioQuantum direct detector. As shown in Extended Data Figs. 3 and 4a, approximately 10,000 movies were collected in 48 h for each dataset, using the AFIS (Aberration-Free Image Shift) system from the software EPU. The data collection details are summarized in Tables 1 and 2.

### Processing

The band patterning in the high-MW area of BN-PAGE is not trivial to deconvolute, and the band intensities do not strictly correspond to the particle distribution on the grids, most probably due to a combination of flexibility and perhaps some SC disassembly upon sample preparation. The processing outline is described in Extended Data Figs. 3, 4a and 8a. Raw micrographs were aligned using the own implementation of motion correction from Relion 3.1 (ref. 64). CTFFIND[65] was used for initial contrast transfer function (CTF) estimation, then Relion 3.1. was used for particle picking, 2D and 3D classification, polishing and CTF/3D refinements, except for per-particle defoci, which were estimated using GCTF[66]. Since the $CIV_S$ and the $CIV_C$ of A-respirasome could not be refined in Relion, the boxed particles were imported in cryoSPARC[67] and refined with local refinement. Postprocessing and local resolution estimation (also done using ResMap) were then performed again in Relion 3.1. To refine the atomic models, the focus-refined maps of CI_PA (peripheral arm), CI_MA (membrane arm), $CIII_2$ and the relevant versions of CIV were fitted into the globally refined maps of each respirasome (to preserve their relative orientations) and merged in Chimera software using 'vop max' command, producing final composite maps. The sections below contain a detailed description of the processing for the different datasets.

### Liver CD1

After optics group assignment, motion correction and CTF estimation of the 9,453 collected movies, 1.8 million particles were picked using LoG picking in Relion, then subjected to 2D classification. Twenty good classes, corresponding to around 1 million particles, were selected and used as 2D references for reference-based picking. This yielded 2.7 million particles, of which 1.1 million (distributed in 19 2D classes) were selected for further processing. The good 2D classes from the two types of picking were then subject to parallel 3D classification, using a previous C-respirasome map filtered to 30 Å, five classes, T4. A total of 742,000 good particles (from four classes) and 851,000 (from three classes) were selected, from LoG and 2D-reference pools, respectively, which were pooled, then subjected to duplicate removal (resulting in 1 million good particles) and per-particle defocus estimation. These 3D classes already showed some density for the various CIV monomers bound around CI, but it was not possible to isolate the three respirasomes at this stage, so the particles were first globally refined, then subjected to signal subtraction, to only keep the regions corresponding

to the weak signal in the 3D classes. The subtracted particles were then classified without alignment, with T64 and five classes, resulting in one class of A-respirasome (57,506 particles) and two classes of $CIV_C$-containing respirasomes (154,760 particles). To maximize the separation of C- and CS-respirasomes, the latter two classes were further classified without alignment with T64 into four classes, which resulted in a class of C-respirasome (103,207 particles) and three classes of CS-respirasome (51,488 particles), different from one another only in the angle between $CIV_S$ and $CIII_2$ and therefore kept together to maximize the signal in focused refinement. The three respirasomes were first globally refined, and then the SC components (CI_PA, CI_MA, $CIII_2$, $CIV_C$ and $CIV_S$) were focus-refined. Since focused refinement did not work for $CIV_C$ from A-respirasome and $CIV_S$ from CS-respirasome, the particles were imported in cryoSPARC and subjected to local refinement, resulting in 3.8 Å maps. All the maps were then postprocessed in Relion, also used to calculate their local resolution. For the FRC on CI (Extended Data Fig. 8a), we focus-refined the peripheral arm of CI from all the good particles, then we classified them without alignment using a loose mask around the membrane arm (T16, six classes) and we refined the resulting single classes to check the conformation of CI.

### Brain CD1

A similar procedure to the one described above for the liver dataset was used to process the brain SCs. In this case, from 10,416 movies, 2 million particles were picked with LoG picking, resulting in six good 2D classes (214,000 particles). The good classes were used as templates for 2D reference-based picking, which resulted in 2.9 million particles, out of which six total good 2D classes (277,000 particles) were selected. Compared to the liver dataset, the brain micrographs were substantially more over-picked. The good 2D classes from LoG picking were 3D classified (T4, six classes), resulting in three good classes, corresponding to a pool of C- and CS-respirasome (class 1), $CICIII_2$ (class 2) and the A-respirasome (class 5). These good 3D classes (containing 87,600 particles in total) were pooled with the good 2D classes from reference-based picking and after duplicate removal 307,000 particles remained, which were subject to 3D classification (T4, five classes). The good particles (159,600 in total) were in this case found in two classes, and subjected to per-particle defocus estimation, CTF-refine, polish and global refinement. After signal subtraction and classification without alignment (T64, six classes) the three respirasomes were isolated and globally refined. Given the low number of particles (17,890 for C-respirasome, 17,248 for CS-respirasome and 12,298 for A-respirasome), local refinement failed, but the global maps coincide well with the structures obtained from liver (Extended Data Fig. 5b), so we did not process these particles further. For the FRC on CI (Extended Data Fig. 8b), we focus-refined the peripheral arm of CI from all the good particles, then classified them without alignment using a loose mask around the membrane arm (T64, six classes) and refined the resulting single classes to check the conformation of CI.

### Structures

The initial models (PDB 6g2j for mouse CI and PDB 7o3c for mouse $CIII_2$ and CIV) were fitted into the combined maps in Chimera. For the $CIV_C$, a COX7A2 AlphaFold[68] model was used and fitted into CIV in the position of SCAF1. The models were subsequently refined in Phenix using a previously designed protocol[5] and manually corrected in Coot[69]. The details about the model statistics are listed in Tables 1 and 2, while representative densities are shown in Extended Data Figs. 5 and 8f,g. Chimera[70] and ChimeraX[71] were used to prepare the figures. Extended Data Table 1 contains the details about the models. MolProbity and EMRinger were used to calculate model statistics.

### Activity

Purified CI in SCs was subject to spectrophotometric activity measurements (reduction of $A_{340}$ as a result of NADH oxidation, coupled to quinone reduction) as described before[43]. CI concentration was calculated using ferricyanide (1 mM) as electron acceptor for NADH oxidation, based on the specific activity of pure CI isolated in LMNG, so that 3–5 µg of complex I was used per measurement. The assay buffer contained 20 mM HEPES pH 7.4, 50 mM NaCl, 1 mM EDTA, 1 mg $ml^{-1}$ BSA, 0.1% digitonin and 0.25 mg $ml^{-1}$ lipid mixture (1:4 cardiolipin:1,2-dioleoyl-*sn*-glycero-3-phosphocholine). For each measurement, 1 ml of assay buffer was pipetted in a cuvette at 30 °C under stirring, to which the protein sample and 200 µM decyl-ubiquinone (DQ) were added. The mixture was incubated for 5 min at 30 °C under stirring to allow DQ diffusion in the micelles, then 100 µM NADH was added to the mixture and the measurement was started, using a Shimadzu UV-2600 ultraviolet–visible spectrophotometer. The A340 curve was recorded for 1–3 min, to completely record the NADH oxidation. Five micromolar rotenone was added to the mixture to measure the baseline curve. The extinction coefficient used to calculate the activity from the absorbance at 340 nm was 6.22. For deactivation, the sample was incubated at 37 °C before the activity measurement. The incubation time was extended to 1 h 45 min to ensure complete deactivation (according to assays with *N*-ethylmaleimide), therefore the activity was not fully recovered after turnover.

### Reporting summary

Further information on research design is available in the Nature Portfolio Reporting Summary linked to this article.

## Data availability

Structures of the three SCs were deposited in PDB (accessions 8PW5, 8PW6 and 8PW7) with corresponding cryo-EM density maps in EMDB (IDs 17989, 17990 and 17991). As the models were built on composite maps, the consensus and focused maps for all components of the three SCs have also been deposited on EMDB (18023, 18022, 18025, 18024, 18027, 18026, 18017, 18018, 18019, 18021, 18020, 18015, 18011, 18012, 18013 and 18014). Similarly, structures of complex I were deposited in PDB (accessions 8RGR, 8RGQ, 8RGP and 8RGT) with corresponding composite cryo-EM density maps (19147, 19146, 19145 and 19148) and consensus/focused maps (19085, 19086, 19087, 19091, 19092, 19093, 19088, 19089, 19090, 19105, 19106 and 19107) in EMDB. The following previously deposited models (PDB codes) have been used in the manuscript: 5gup, 5xth, 5iy5, 1ooc, 5z62, 3cx5, 7o3c, 5j4z, 5j7y, 7o37 and 6g2j. Uncropped gels and western blot, as well as the raw data for the activity assays summarized in Extended Data Fig. 8h, have been provided as Source data in this publication. Source data are provided with this paper.

## References


59. Smith, A. L. [13] Preparation, properties, and conditions for assay of mitochondria: slaughterhouse material, small-scale. *Methods Enzymol.* **10**, 81–86 (1967).
60. Stepanova, A. et al. The dependence of brain mitochondria reactive oxygen species production on oxygen level is linear, except when inhibited by antimycin A. *J. Neurochem.* **148**, 731–745 (2019).
61. Kun, E., Kirsten, E. & Piper, W. N. Stabilization of mitochondrial functions with digitonin. *Methods Enzymol.* **55**, 115–118 (1979).
62. Wittig, I., Karas, M. & Schägger, H. High resolution clear native electrophoresis for in-gel functional assays and fluorescence studies of membrane protein complexes. *Mol. Cell. Proteom.* **6**, 1215–1225 (2007).
63. Kampjut, D., Steiner, J. & Sazanov, L. A. Cryo-EM grid optimisation for membrane proteins. *iScience* **24**, 102139 (2021).
64. Zivanov, J., Nakane, T. & Scheres, S. H. W. Estimation of high-order aberrations and anisotropic magnification from cryo-EM data sets in RELION-3.1. *IUCrJ* **7**, 253–267 (2020).

65. Rohou, A. & Grigorieff, N. CTFFIND4: fast and accurate defocus estimation from electron micrographs. *J. Struct. Biol.* **192**, 216–221 (2015).
66. Zhang, K. Gctf: real-time CTF determination and correction. *J. Struct. Biol.* **193**, 1–12 (2016).
67. Punjani, A., Rubinstein, J. L., Fleet, D. J. & Brubaker, M. A. cryoSPARC: algorithms for rapid unsupervised cryo-EM structure determination. *Nat. Methods* **14**, 290–296 (2017).
68. Jumper, J. et al. Highly accurate protein structure prediction with AlphaFold. *Nature* **596**, 583–589 (2021). *2021 596:7873*.
69. Emsley, P., Lohkamp, B., Scott, W. G. & Cowtan, K. Features and development of Coot. *Acta Crystallogr. D* **66**, 486–501 (2010).
70. Pettersen, E. F. et al. UCSF Chimera—a visualization system for exploratory research and analysis. *J. Comput. Chem.* **25**, 1605–1612 (2004).
71. Pettersen, E. F. et al. UCSF ChimeraX: structure visualization for researchers, educators, and developers. *Protein Sci.* **30**, 70–82 (2021).

## Acknowledgements

This research was supported by the Scientific Service Units (SSU) of IST Austria through resources provided by the Electron Microscopy Facility (EMF), the Life Science Facility (LSF), the Pre-Clinical Facility (PCF) and the IST high-performance computing cluster. The authors also acknowledge O. Petrova for her help with the complex I data acquisition. I.V. is funded by the ERC Advanced Grant 101020697 RESPICHAIN to L.S. The funders had no role in study design, data collection and analysis, decision to publish or preparation of the manuscript.

## Author contributions

I.V. and L.A.S. designed the project. I.V. purified the samples, prepared cryo-EM grids, acquired and processed EM data, built and analyzed the atomic models and wrote the initial draft of the manuscript. L.A.S. acquired funding, supervised the project, analyzed data and models and revised the manuscript.

## Competing interests

The authors (I.V. and L.A.S.) declare no competing interests.

## Additional information

**Extended data** is available for this paper at https://doi.org/10.1038/s41594-024-01255-0.

**Supplementary information** The online version contains supplementary material available at https://doi.org/10.1038/s41594-024-01255-0.

**Correspondence and requests for materials** should be addressed to Leonid A. Sazanov.

**Peer review information** *Nature Structural & Molecular Biology* thanks the anonymous reviewer(s) for their contribution to the peer review of this work. Dimitris Typas was the primary editor on this article and managed its editorial process and peer review in collaboration with the rest of the editorial team.

https://doi.org/10.1038/s41594-024-01255-0

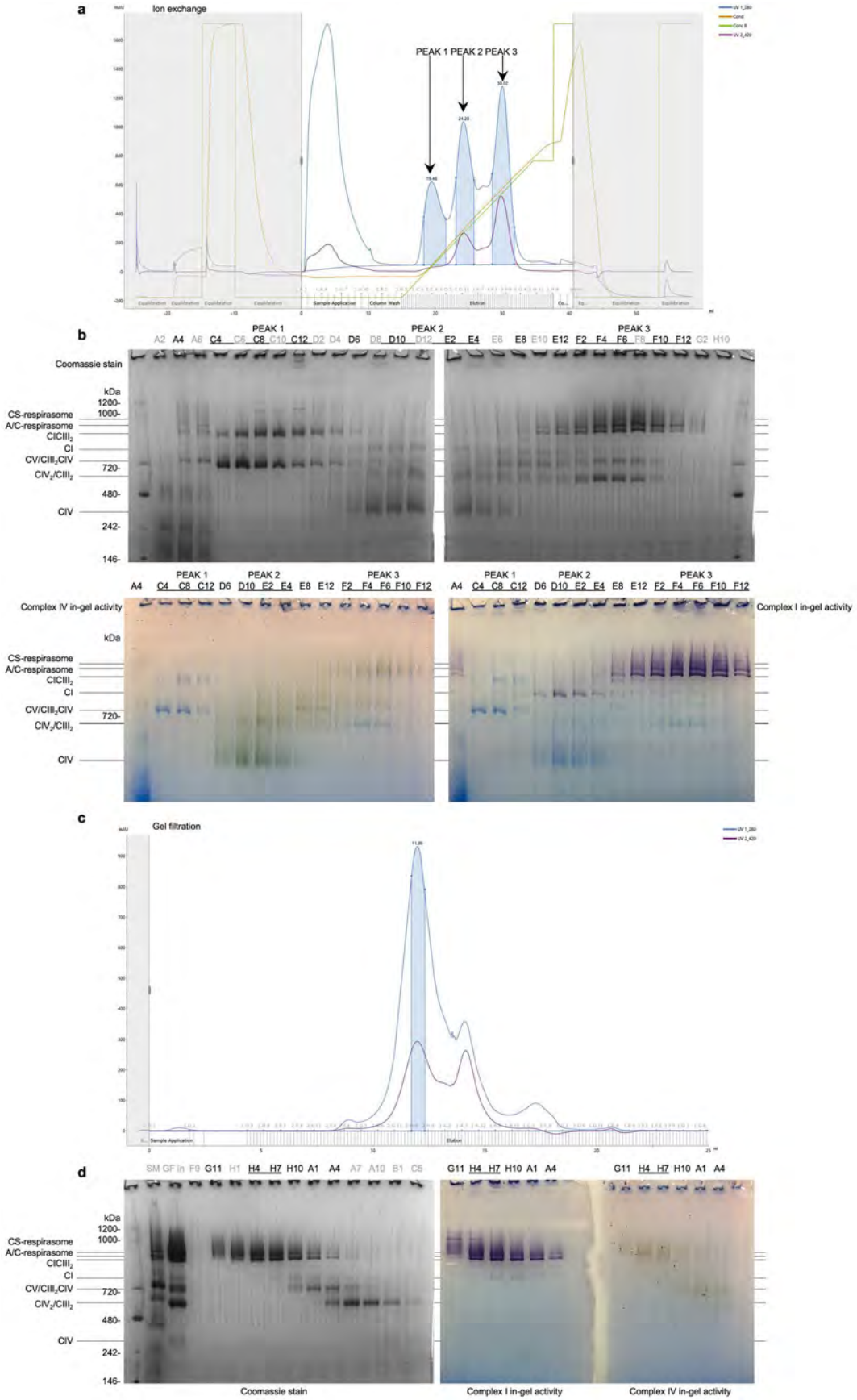


**Extended Data Fig. 1 | Representative purification. a**. Ion exchange chromatography and **c**. gel filtration profiles with **b**. and **d**. respective BN-PAGE of the resulting fractions. (**b**) Coomassie stain on top and in-gel activity at the bottom, left for CIV and right for CI and (**d**) Coomassie stain on left, in-gel activity for CI in the middle and for CIV on the right. Peak 3 from the ion exchange was selected and subjected to gel filtration. MW markers are indicated on the left. The experiment was repeated at least three times independently with similar results.

https://doi.org/10.1038/s41594-024-01255-0

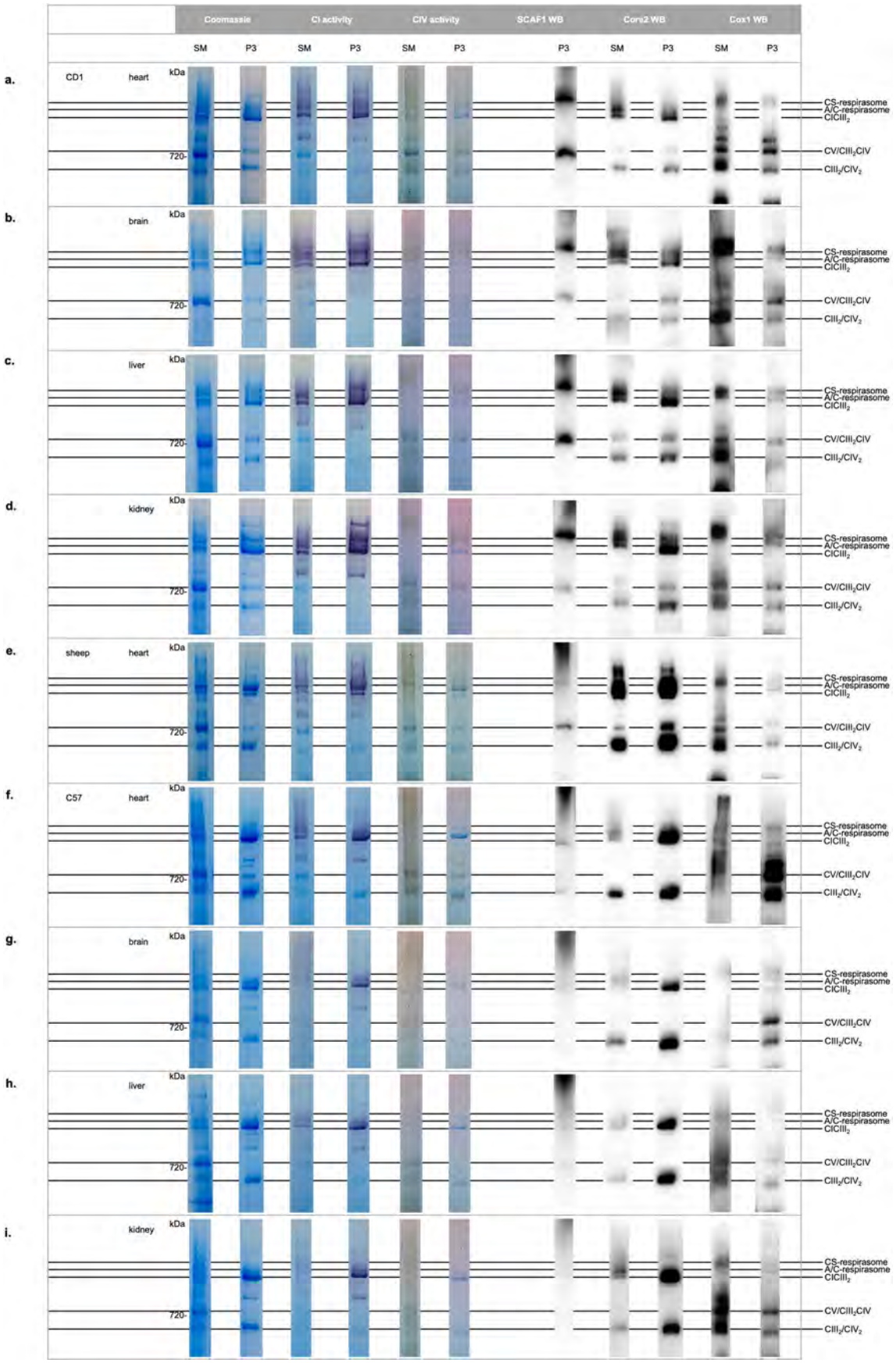


**Extended Data Fig. 2 | Distribution of supercomplexes across tissues, murine strains and mammalian species.** BN-PAGE runs of CD1 mice hearts (**a**), brains (**b**), livers (**c**), kidneys (**d**), sheep heart (**e**) C57 mice hearts (**f**), brains (**g**), livers (**h**), kidneys (**i**), stained as indicated on top of the figure. SM is solubilised material, P3 is peak 3 of the MonoQ run, WB is Western Blot. The different species are indicated on the right for each section, and the position of 720 kDa MW marker on the left, for clarity. The experiment was repeated at least three times independently with similar results.

https://doi.org/10.1038/s41594-024-01255-0

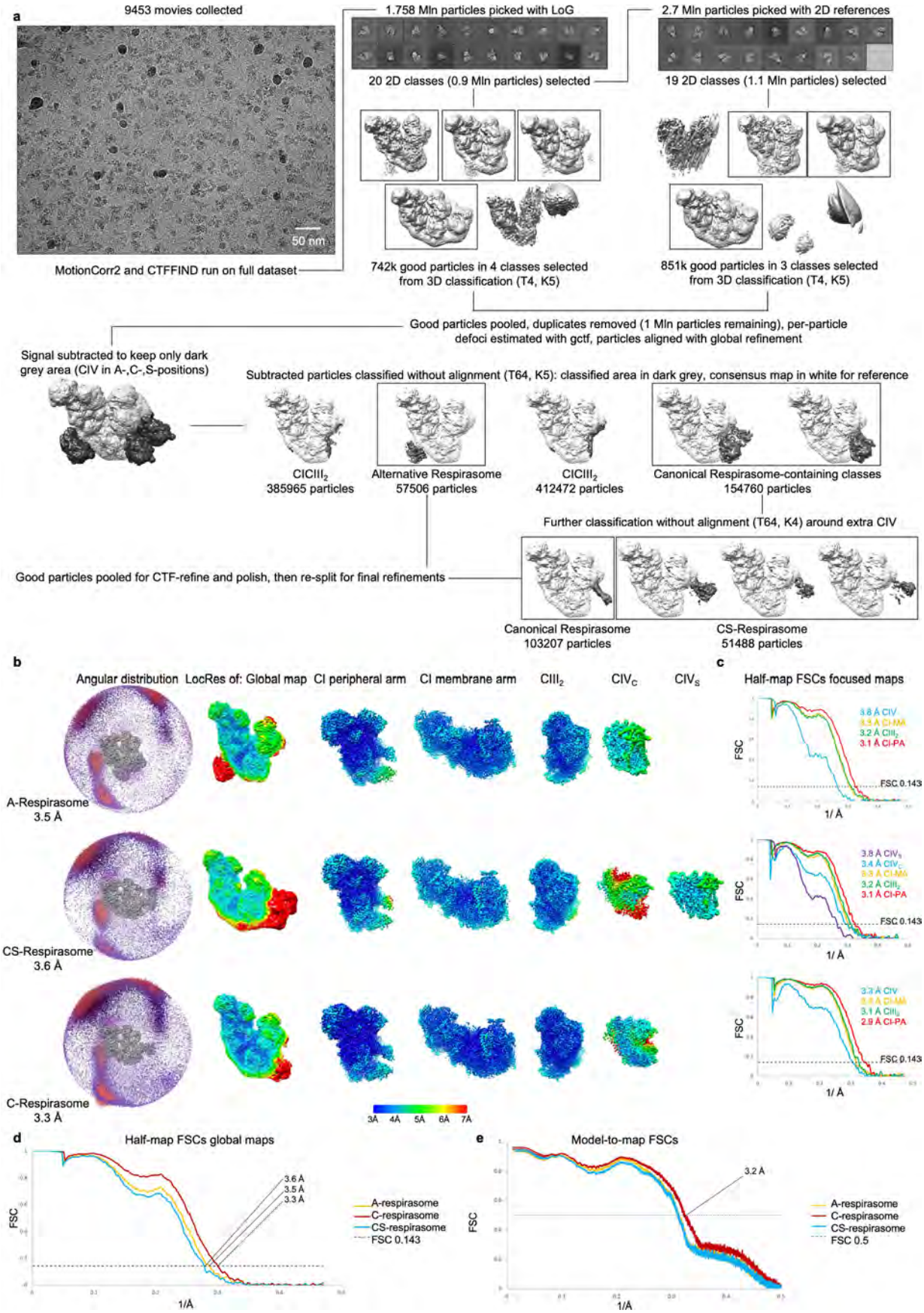


**Extended Data Fig. 3 | Processing of CD1 liver dataset.** Schematic view of the processing pipeline for the CD1 liver dataset, as explained in the Methods section (**a**), with angular distribution, locally filtered global and focused maps (**b**), final Fourier Shell Correlation (FSC) graphs for focused maps (**c**), global maps (**d**) and models (**e**).

https://doi.org/10.1038/s41594-024-01255-0

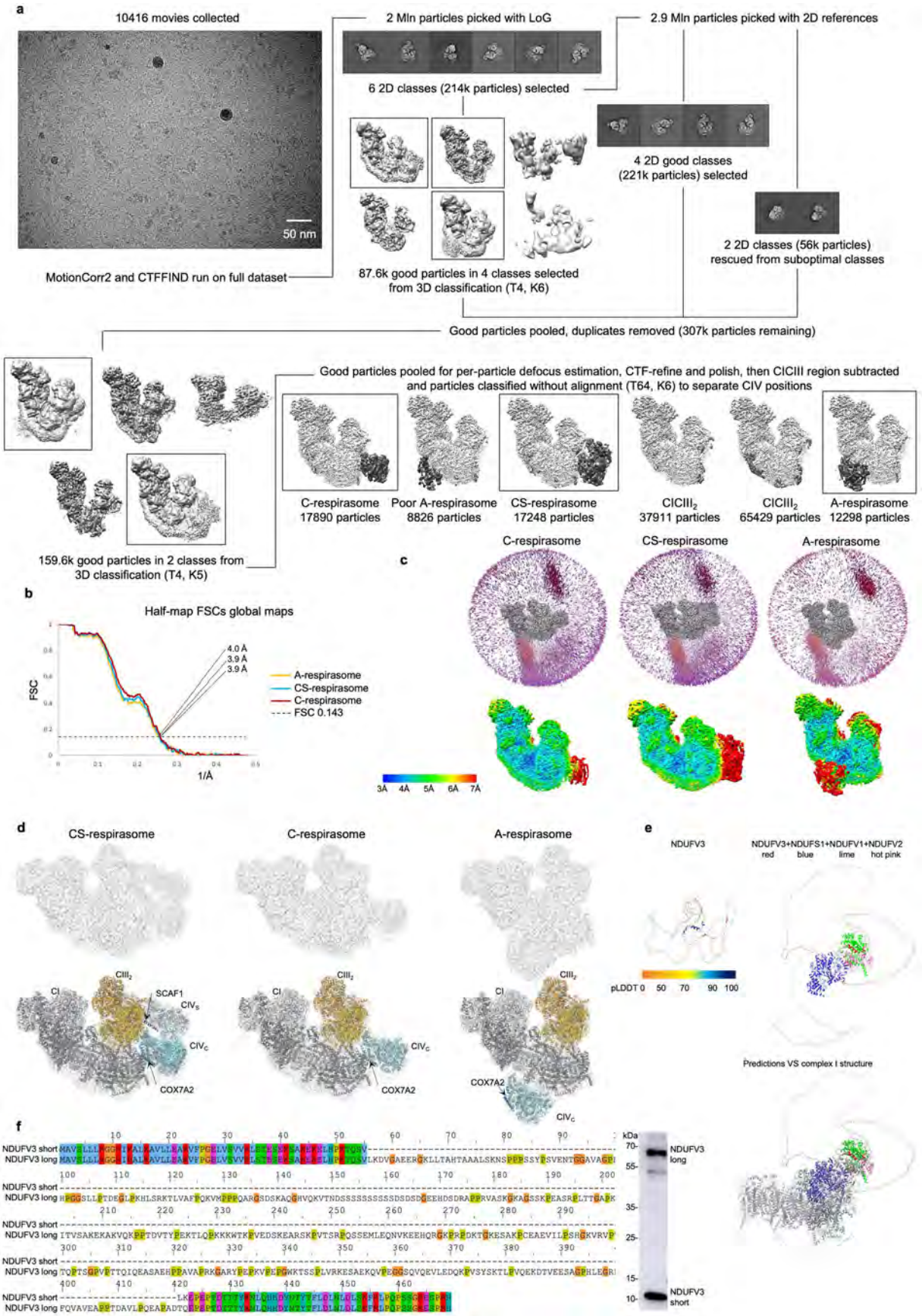


**Extended Data Fig. 4 | See next page for caption.**

https://doi.org/10.1038/s41594-024-01255-0

**Extended Data Fig. 4 | Processing of CD1 brain dataset and map features.** **a**. Schematic view of the processing pipeline for the CD1 brain dataset, as explained in the Methods section, with **b**. final Fourier Shell Correlation (FSC) graphs for the global maps and **c**. angular distribution and locally filtered global maps. **d**. Respirasome models derived from the liver dataset fitted into the brain maps. Maps shown in light grey on top by themselves and on bottom with fitted models, coloured as throughout the manuscript and shown as secondary structures. **e**. Alphafold2 (top left, coloured by confidence values) and Alphafold multimer (top right, four subunits forming NADH-binding domain, coloured by chain) prediction for the structure of the long isoform of NDUFV3, overlaid to the full CI structure (bottom, with full CI in grey). **f**. Analysis of NDUFV3 long and short isoforms. Left, sequence alignment, where the first 35 residues represent the mitochondrial targeting sequence and the subsequent 25 residues are disordered in short isoform-containing samples, with only ~43 C-terminal residues ordered. Right, western blot of brain CI sample. The experiment was repeated on two independent brain preparation, plus one preparation on different tissues (ovine/murine heart and murine liver) with similar results.

https://doi.org/10.1038/s41594-024-01255-0

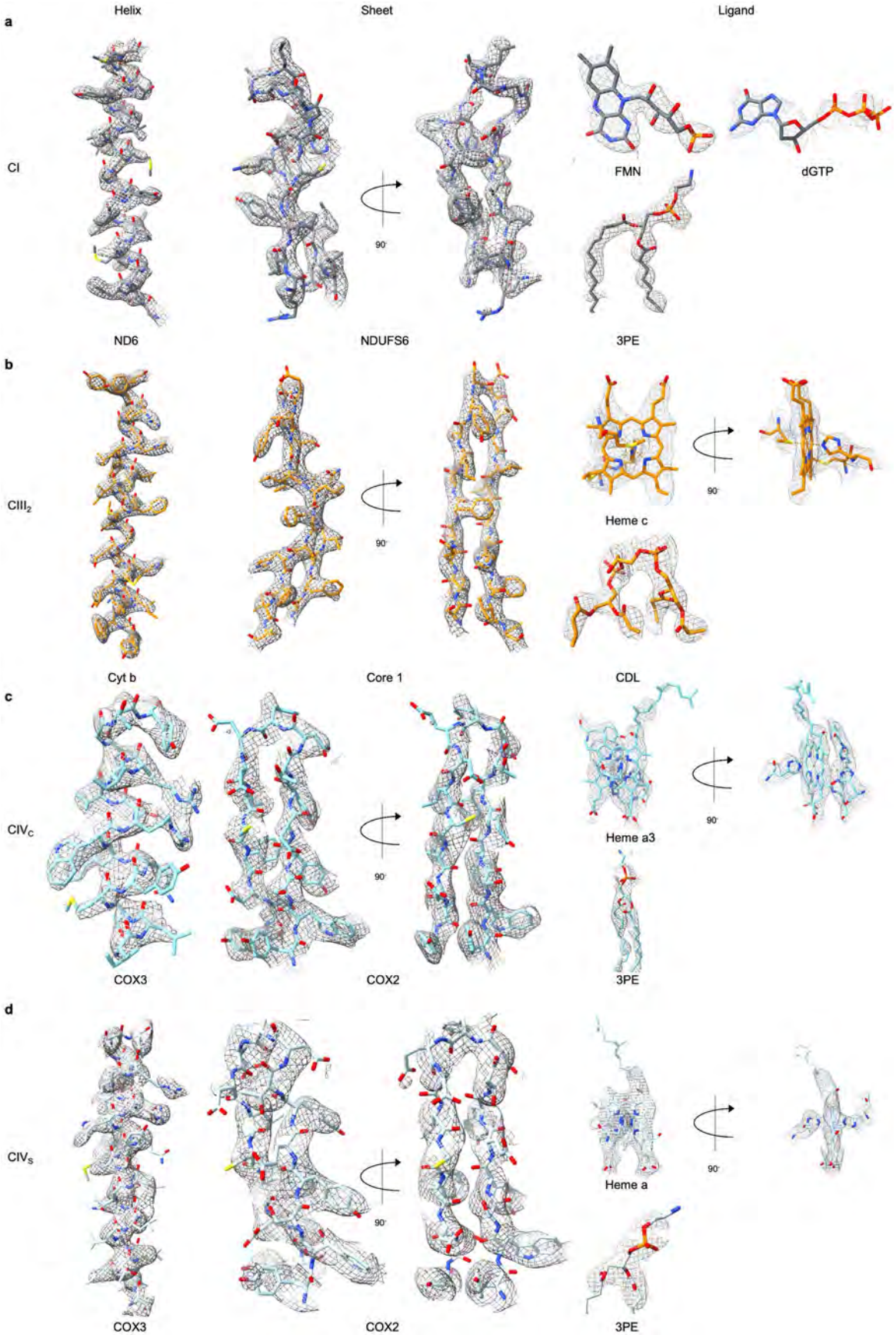


**Extended Data Fig. 5 | Representative densities from the respirasomes models.** Representative densities for CI (**a**), $CIII_2$ (**b**), $CIV_C$ (**c**) and $CIV_S$ (**d**): for each an alpha helix, a beta sheet, a ligand and a lipid are shown. For CI, dGTP is shown in addition to FMN.

https://doi.org/10.1038/s41594-024-01255-0

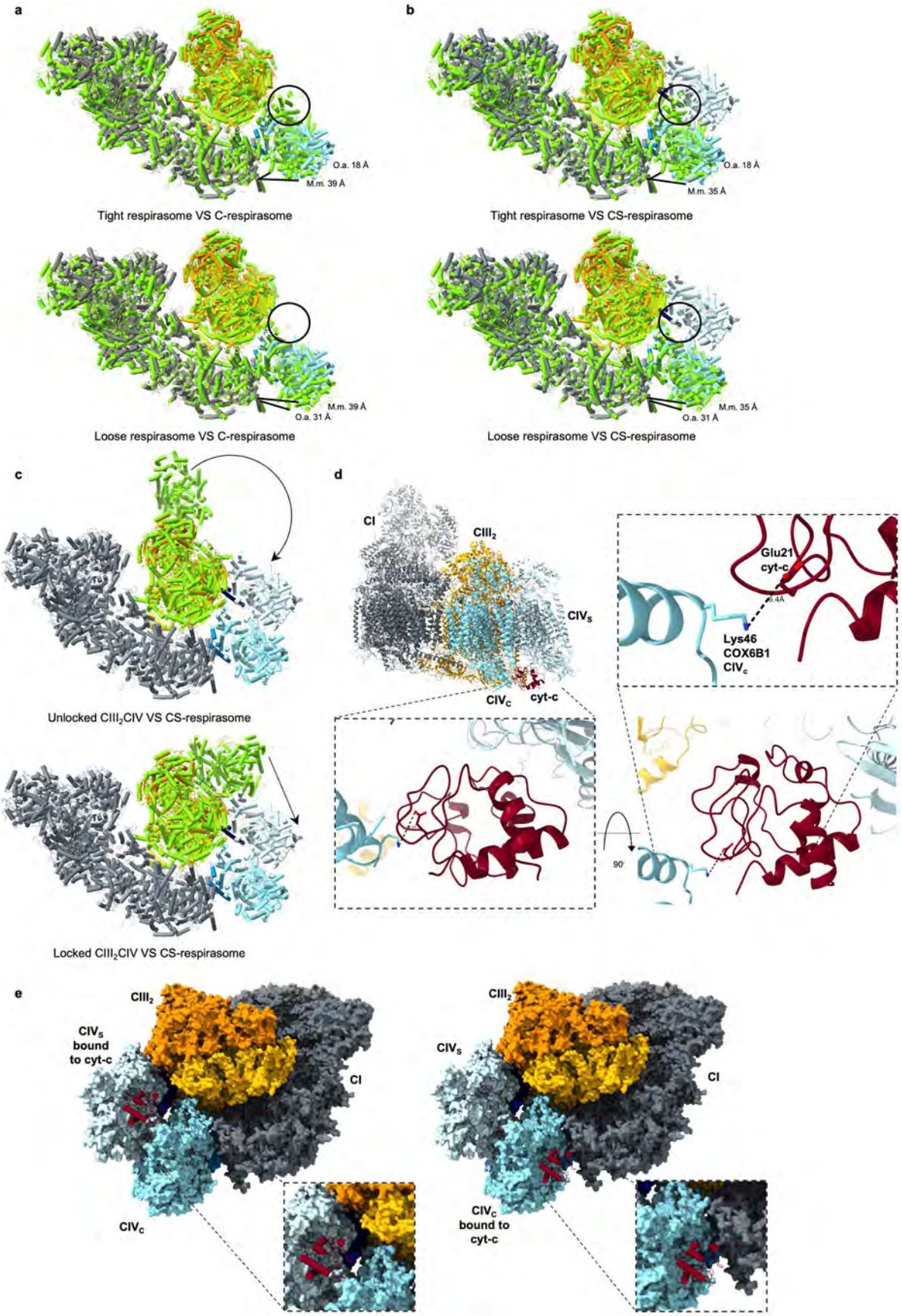


**Extended Data Fig. 6 | See next page for caption.**

https://doi.org/10.1038/s41594-024-01255-0

**Extended Data Fig. 6 | CIV conformations and cytochrome c binding in respirasomes. a-c.** Superposition of the structures solved in this manuscript from murine liver (shown as secondary structures with piped helices and coloured as in the other figures, that is CI grey, $CIII_2$ yellow and orange, $CIV_C$ cyan with COX7A2 light blue, $CIV_S$ ice with SCAF1 dark blue) to the other known mammalian supercomplexes featuring CIV (shown as secondary structures with piped helices and coloured in green). VS is versus. **a.** Superposition of the murine C-respirasome to the tight (top, PDB 5j4z) and loose (bottom, PDB 5j7y) respirasome from ovine heart, aligned on the membrane arm of CI. The circle highlights the CIV shift between tight and loose conformation. **b.** Superposition of the CS-respirasome to the tight (top, PDB 5j4z) and loose (bottom, PDB 5j7y) respirasome from ovine heart, aligned on the membrane arm of CI, as in **a**. As in **a**, the circles highlight the CIV shift between tight and loose conformation, outlining the region of $CIV_C$ clashing between the tight conformation of CIV in the ovine respirasome and the $CIV_S$ of the CS-respirasome (top panel). The distance between the edge helices of CI and CIV, depicted by the black lines, is measured in Å in each panel for the ovine (*O.a.*) and murine (*M.m.*) supercomplexes shown. In **a**, the difference in CI-to-CIV distance is 39-31=8 Å between murine C-respirasome and ovine loose respirasome and 39-18=21 Å between murine C-respirasome and ovine tight respirasome. In **b**, this is 35-31=4 Å between murine CS-respirasome and ovine loose and 35-18=17 Å between murine CS-respirasome and ovine tight. **c.** Superposition of the CS-respirasome to the unlocked mature (top, PDB 7o3c) and locked (bottom, PDB 7o37) $CIII_2CIV$ from murine heart, aligned on SCAF1-containing CIII monomer. The arrows indicate the displacement of $CIV_S$. **d-e.** Cyt-c binding sites of CS-respirasome. In **d**, the putative contact between cyt-c bound to $CIV_S$ and Lys 46 of COX6B1 on $CIV_C$ is depicted: the insets show zoomed-in views of the binding site. In **e**, the binding sites of cyt-c on $CIV_S$ (left) and $CIV_C$ (right) are shown. In both panels, cyt-c is docked based on PDB 5iy5, complexes are coloured as in the rest of the manuscript, cyt-c is burgundy.

https://doi.org/10.1038/s41594-024-01255-0

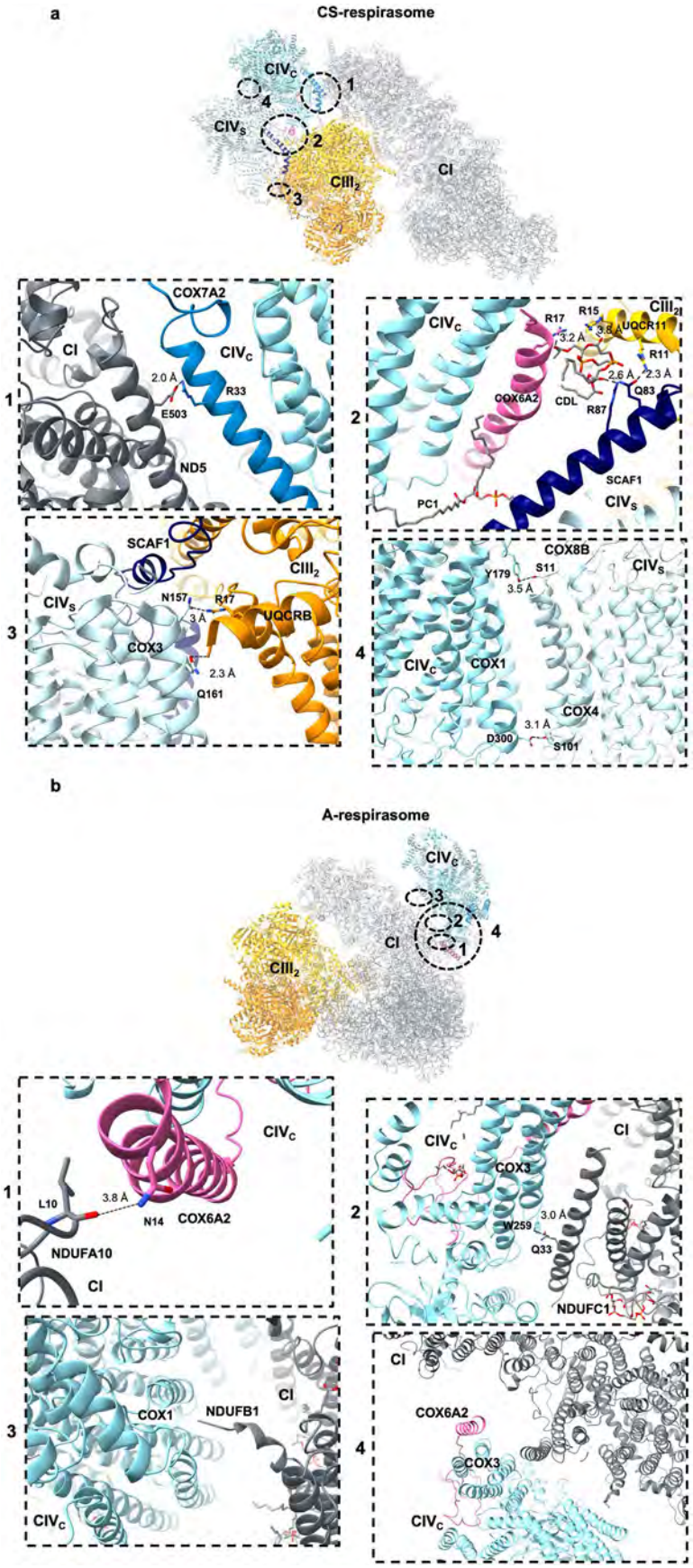


**Extended Data Fig. 7 | Interfaces of respirasomes.** Newly-found interaction interfaces in the CS- (**a**) and A- (**b**) respirasomes: the details are shown in the insets. CDL is cardiolipin, PC1 is phosphatidylcholine. The complexes are coloured as in the rest of the manuscript, COX6A2 is hot pink and all the lipids are grey.

https://doi.org/10.1038/s41594-024-01255-0

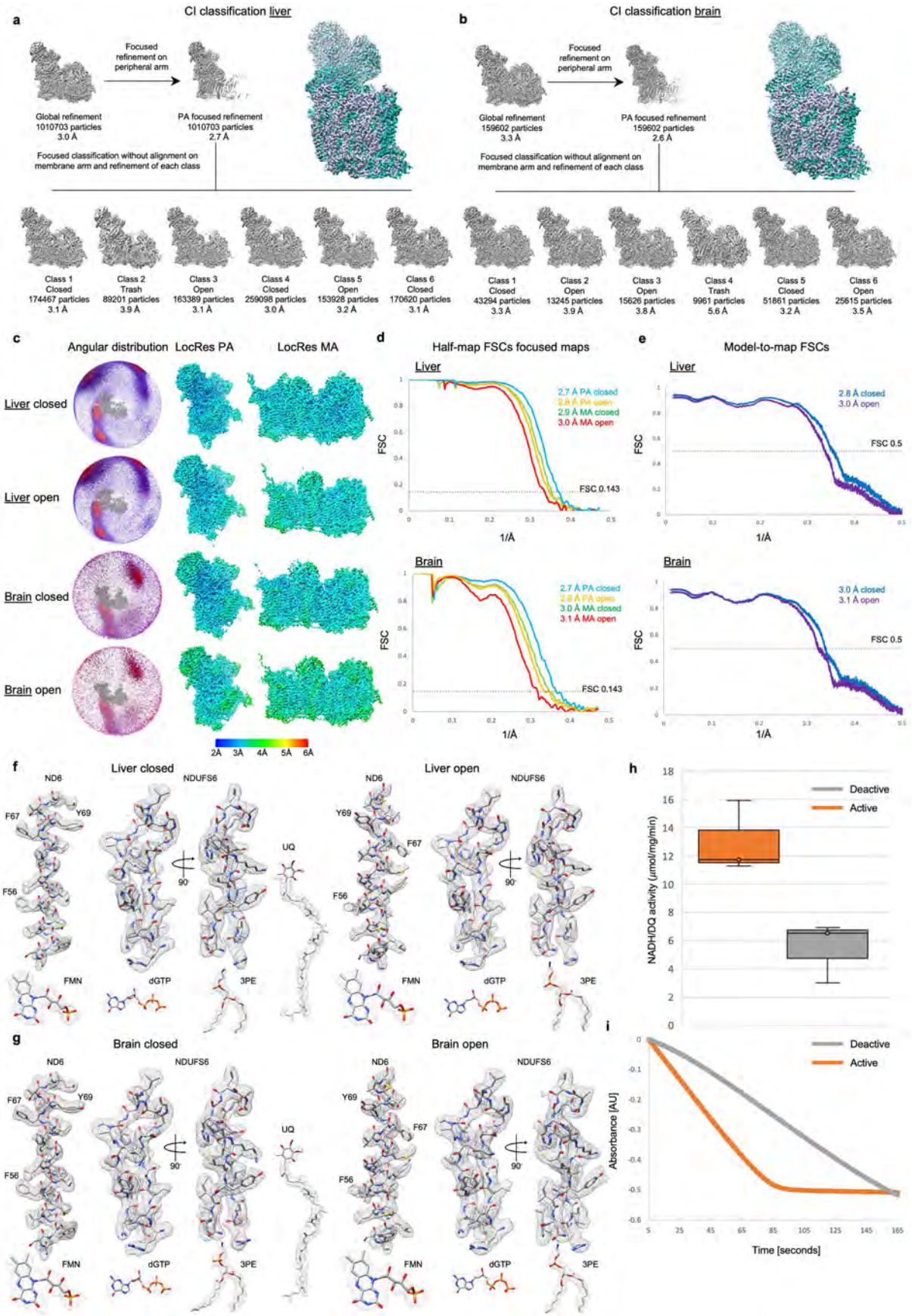


**Extended Data Fig. 8 | See next page for caption.**

https://doi.org/10.1038/s41594-024-01255-0

**Extended Data Fig. 8 | Complex I structure determination and features.** **a**-**b**. Processing overview of CI particles from the liver (**a**) and brain (**b**) datasets as described in the Methods section. Representative open (light sea green) and closed (lilac) classes are overlaid in the insets, aligned on the peripheral arm, to highlight the difference in CI conformation between them, used for classification in Focus-Reverse-Classify method. **c**-**e**. Final resulting maps, including angular distribution and local resolution (**c**), half-map FSCs (**d**) and map-to-model FSCs (**e**). PA is peripheral arm, MA is membrane arm. **f**-**g**. Representative densities for CI from liver (**f**), and brain (**g**): as for the other supercomplexes, an alpha helix, a beta sheet, dGTP and FMN ligands and a lipid are shown for closed and open states. For the closed state of liver and brain complex I the quinone density (UQ) is also shown. **h**-**i**. CI activity, measured as reduction of $A_{340}$ absorbance over time due to NADH oxidation. In **h**, the graph shows the result of three independent purifications from CD1 livers. In the box and whiskers representation, minimum and maximum values are indicated as top and bottom lines; the coloured squares are delimited by first and third quartiles and contain the median value as line with empty dot inside. As the representation results from three independent experiments, the minimum, median and maximum values shown correspond to the individual measurements. No error bars are shown, as no statistical analysis was performed. **i** shows a representative replicate with raw traces. Active (as prepared) CI is orange, deactive (heated to 37° C for 105 min without substrates, Methods) is grey.

https://doi.org/10.1038/s41594-024-01255-0

## Extended Data Table 1 | Model composition (CS-respirasome used)

| | Subunit name (alias) | Chain ID | Range built/total residues | Un-modelled residues | % modelled residues | Cofactors | Notes |
|---|---|---|---|---|---|---|---|
| Complex I core subunits | MT-ND3 (ND3) | A1 | 1-115/115 | - | 100.0 | | N-formyl Met |
| | NDUFS7 (PSST) | 6 | 33-189/189 | 1-32 | 83.0 | N2 (4Fe) | |
| | NDUFS3 (30 kDa) | C1 | 7-214/228 | 1-6,215-228 | 91.2 | | |
| | NDUFS2 (49 kDa) | D1 | 1-430/430 | - | 100.0 | | Dimethylated Arg85 |
| | NDUFV2 (24 kDa) | 2 | 4-217/217 | 1-3 | 98.6 | N1a (2Fe) | |
| | NDUFV1 (51 kDa) | 1 | 9-438/444 | 1-8,439-444 | 96.8 | FMN, N3 (4Fe) | |
| | NDUFS1 (75 kDa) | 3 | 5-684/704 | 1-4,695-704 | 98.0 | N1b (2Fe), N4 (4Fe), N5 (4Fe) | |
| | MT-ND1 (ND1) | H1 | 1-318/318 | - | 100.0 | | N-formyl Met |
| | NDUFS8 (TYKY) | 9 | 1-178/178 | - | 100.0 | N6a (4Fe), N6b (4Fe) | |
| | MT-ND6 (ND6) | J1 | 1-172/172 | - | 100.0 | | N-formyl Met |
| | MT-ND4L (ND4L) | K1 | 1-98/98 | - | 100.0 | | N-formyl Met |
| | MT-ND5 (ND5) | L1 | 1-606/607 | 607 | 99.8 | | N-formyl Met |
| | MT-ND4 (ND4) | M1 | 1-459/459 | - | 100.0 | | N-formyl Met |
| | MT-ND2 (ND2) | N1 | 1-345/345 | - | 100.0 | | N-formyl Met |
| Complex I supernumerary subunits | NDUFA10 (42 kDa) | O1 | 1-320/320 | - | 100.0 | dGTP | |
| | NDUFA9 (39 kDa) | P1 | 1-342/342 | - | 100.0 | NADPH | |
| | NDUFS4 (18 kDa) | Q1 | 8-133/133 | 1-7 | 94.7 | | |
| | NDUFS6 (13 kDa) | 7 | 1-96/96 | - | 100.0 | $Zn^{2+}$ | |
| | NDUFA2 (B8) | S1 | 13-96/99 | 1-12,97-99 | 84.8 | | |
| | NDUFAB1 (SDAP$\alpha/\beta$) | T1 U1 | 6-84/88 1-88/88 | 1-5,85-88 - | 89.8 100.0 | Phospho-pantetheine | |
| | NDUFA5 (B13) | V1 | 3-115/115 | 1-2 | 98.3 | | |
| | NDUFA6 (B14) | W1 | 17-130/130 | 1-16 | 87.7 | | |
| | NDUFA8 (PGIV) | X1 | 1-171/171 | - | 100.0 | | |
| | NDUFA11 (B14.7) | Y1 | 1-140/140 | - | 100.0 | | |
| | NDUFA13 (B16.6) | Z1 | 3-143/143 | 1-2 | 98.6 | | |
| | NDUFA1 (MWFE) | a1 | 1-70 | - | 100.0 | | |
| | NDUFA3 (B9) | b1 | 1-83/83 | - | 100.0 | | N-acetyl Ala |
| | NDUFC1 (KFYI) | c1 | 1-48/49 | 49 | 98.0 | | |
| | NDUFC2 (B14.5b) | d1 | 1-120/120 | - | 100.0 | | |
| | NDUFS5 (15 kDa) | e1 | 1-105/105 | - | 100.0 | | |
| | NDUFB1 (MNLL) | f1 | 5-57/57 | 1-4 | 93.0 | | |
| | NDUFB11 (ESSS) | g1 | 21-121/122 | 1-20,122 | 82.7 | | |
| | NDUFB5 (SGDH) | h1 | 5-143/143 | 1-4 | 97.2 | | |
| | NDUFB6 (B17) | i1 | 1-35,57-127/127 | 36-56 | 83.5 | | N-acetyl Ser 36-56 unresolved |
| | NDUFB2 (AGGG) | j1 | 5-69/72 | 1-4,70-72 | 90.3 | | |
| | NDUFB3 (B12) | k1 | 18-94/103 | 1-17,95-103 | 74.8 | | |
| | NDUFB8 (ASHI) | l1 | 1-157/157 | - | 100.0 | | |
| | NDUFB4 (B15) | m1 | 3-128/128 | 1-2 | 98.4 | | |
| | NDUFB9 (B22) | n1 | 1-178/178 | - | 100.0 | | |
| | NDUFB7 (B18) | o1 | 1-118/136 | 119-136 | 86.8 | | |
| | NDUFB10 (PDSW) | p1 | 2-171/175 | 1,172-175 | 97.1 | | |
| | NDUFA12 (B17.2) | q1 | 1-145/145 | - | 100.0 | | |
| | NDUFA7 (B14.5a) | r1 | 1-76,90-112/112 | 77-89 | 89.3 | | N-acetyl Ala |
| | NDUFV3 (10 kDa) | s1 | 27-68/69 | 1-26,69 | 60.9 | | |
| Complex III | UQCRC1 (Core1) | A L | 2-446/446(A) 2-446/446(L) | 1(A) 1(L) | 99.8(A) 99.8(L) | | |
| | UQCRC2 (Core2) | B M | 20-439/439 20-439/439 | 1-19 1-19 | 95.7 95.7 | | |
| | MT-CYB | C N | 1-380/381 1-380/381 | 381 381 | 99.5 99.5 | Heme $b_L$ Heme $b_H$ | |
| | CYC1 | D O | 1-240/241 1-240/241 | 241 241 | 99.6 99.6 | Heme $c_1$ | |
| | UQCRFS1 (ISP) | E P | 1-196/196 1-196/196 | - - | 100.0 100.0 | 2Fe-2S cluster | Ordered density until residue 72 |
| | UQCRB (Sub6) | F Q | 13-110/110 9-110/110 | 1-12 1-8 | 89.1 92.7 | | |
| | UQCRQ (Sub7) | G R | 2-78/81 2-78/81 | 1,79-81 1,79-81 | 95.1 95.1 | | |
| | UQCRH (Sub8) | H S | 11-76/76 9-76/76 | 1-10 1-8 | 86.8 89.5 | | |
| | UQCR10 (Sub10) | J U | 2-61/63 2-61/63 | 1,62-63 1,62-63 | 95.2 95.2 | | |
| | UQCR11 (Sub11) | K V | 2-53/56 1-53/56 | 1,54-56 54-56 | 92.9 94.6 | | |
| | Sub9 | T | 1-78/78 | - | 100.0 | | a.k.a. N-terminus of ISP precursor |
| SCAF1 | COX7A2L | I | 1-111/113 | 112-113 | 98.2 | | N-ter in CIII, C-ter in CIV, PolyAla 31-53 |
| Complex IV | MT-CO1 | a n | 1-514/514 1-514/514 | - - | 100.0 100.0 | $Cu_B$, $Na^+$, Heme $a/a_3$ | |
| | MT-CO2 | b o | 1-227/227 1-227/227 | - - | 100.0 | $Cu_A$, $Mg^{2+}$ | |
| | MT-CO3 | c p | 3-261/261 2-261/261 | 1-2 1 | 99.2 99.6 | | |
| | COX4I1 | d q | 8-146/147 8-146/147 | 1-7,147 1-7,147 | 94.6 94.6 | | |
| | COX5A | e r | 7-109/109 6-109/109 | 1-6 1-5 | 94.5 95.4 | | |
| | COX5B | f s | 5-97/99 4-97/99 | 1-4,98-99 1-3,98-99 | 93.6 95.0 | $Zn^{2+}$ | |
| | COX6A2 | g t | 10-84/85 10-84/85 | 1-9,85 1-9,85 | 88.2 88.2 | | |
| | COX6B1 | h u | 7-85/85 7-85/85 | 1-6 1-6 | 92.9 92.9 | | |
| | COX6C | i v | 4-75/75 5-75/75 | 1-3 1-4 | 96.0 94.7 | | |
| | COX7B | k x | 7-54/56 6-54/56 | 1-6,55-56 1-5,55-56 | 85.7 87.5 | | |
| | COX7C | l y | 2-47/47 1-47/47 | 1 - | 97.9 100.0 | | |
| | COX8B | m z | 1-43/46 1-43/46 | 44-46 44-46 | 93.5 93.5 | | |
| | COX7A2 | w | 1-57/60 | 58-60 | 95.0 | | Present only in $CIV_C$ |
| **total** | | | **15959/16451** | **492** | **97.0 %** | **CS-respirasome** | |

The features of the atomic model of the CS respirasome are listed.

nature portfolio

Corresponding author(s): Leonid Sazanov

Last updated by author(s): Jan 23, 2024

# Reporting Summary

Nature Portfolio wishes to improve the reproducibility of the work that we publish. This form provides structure for consistency and transparency in reporting. For further information on Nature Portfolio policies, see our Editorial Policies and the Editorial Policy Checklist.

## Statistics

For all statistical analyses, confirm that the following items are present in the figure legend, table legend, main text, or Methods section.

| n/a | Confirmed |
|---|---|
| ☐ | ☒ The exact sample size (*n*) for each experimental group/condition, given as a discrete number and unit of measurement |
| ☐ | ☒ A statement on whether measurements were taken from distinct samples or whether the same sample was measured repeatedly |
| ☒ | ☐ The statistical test(s) used AND whether they are one- or two-sided<br>*Only common tests should be described solely by name; describe more complex techniques in the Methods section.* |
| ☒ | ☐ A description of all covariates tested |
| ☒ | ☐ A description of any assumptions or corrections, such as tests of normality and adjustment for multiple comparisons |
| ☒ | ☐ A full description of the statistical parameters including central tendency (e.g. means) or other basic estimates (e.g. regression coefficient) AND variation (e.g. standard deviation) or associated estimates of uncertainty (e.g. confidence intervals) |
| ☒ | ☐ For null hypothesis testing, the test statistic (e.g. *F*, *t*, *r*) with confidence intervals, effect sizes, degrees of freedom and *P* value noted<br>*Give P values as exact values whenever suitable.* |
| ☒ | ☐ For Bayesian analysis, information on the choice of priors and Markov chain Monte Carlo settings |
| ☒ | ☐ For hierarchical and complex designs, identification of the appropriate level for tests and full reporting of outcomes |
| ☒ | ☐ Estimates of effect sizes (e.g. Cohen's *d*, Pearson's *r*), indicating how they were calculated |

*Our web collection on statistics for biologists contains articles on many of the points above.*

## Software and code

Policy information about availability of computer code

| | |
|---|---|
| Data collection | FEI EPU 1.10 |
| Data analysis | MotionCor2, CTFFIND4, GCTF 1.06, RELION 3.1, Chimera 1.13.1, ChimeraX-1.6.1, Coot 0.8.9, Phenix 1.20, ResMap 5.0, MolProbity 4, EMRinger (embedded in Phenix 1.20), AlphaFold2 ( https://t.ly/88mUv), AlphaFold multimer (Cosmic cryo-EM platform https://cosmic-cryoem.org/tools/alphafoldmultimer/), cryoSPARC v4. |

For manuscripts utilizing custom algorithms or software that are central to the research but not yet described in published literature, software must be made available to editors and reviewers. We strongly encourage code deposition in a community repository (e.g. GitHub). See the Nature Portfolio guidelines for submitting code & software for further information.

## Data

Policy information about availability of data

All manuscripts must include a data availability statement. This statement should provide the following information, where applicable:

- Accession codes, unique identifiers, or web links for publicly available datasets
- A description of any restrictions on data availability
- For clinical datasets or third party data, please ensure that the statement adheres to our policy

Structures of the three supercomplexes were deposited in PDB (access IDs 8PW5, 8PW6, 8PW7) with corresponding cryo-EM density maps in EMDB (IDs 17989, 17990, 17991). As the models were built on composite maps, the consensus and focused maps for all components of the three supercomplexes have also been deposited on EMDB (18023, 18022, 18025, 18024, 18027, 18026, 18017, 18018, 18019, 18021, 18020, 18015, 18011, 18012, 18013, 18014).
Similarly, structures of complex I were deposited in PDB (access IDs 8RGR, 8RGQ, 8RGP, 8RGT) with corresponding cryo-EM density maps (19147, 19146, 19145, 19148) and consensus/focused maps (19085, 19086, 19087, 19091, 19092, 19093, 19088, 19089, 19090, 19105, 19106, 19107) in EMDB.
The following previously deposited models (PDB codes) have been used in the manuscript: 5gup, 5xth, 5iy5, 1ooc, 5z62, 3cx5, 7o3c, 5j4z, 5j7y, 7o37, 6g2j.
Uncropped gels and western blot, as well as the raw data for the activity assays summarised in Extended Data Fig 8h, have been provided as Source Data in this publication.

## Research involving human participants, their data, or biological material

Policy information about studies with human participants or human data. See also policy information about sex, gender (identity/presentation), and sexual orientation and race, ethnicity and racism.

| | |
|---|---|
| Reporting on sex and gender | n.a. |
| Reporting on race, ethnicity, or other socially relevant groupings | n.a. |
| Population characteristics | n.a. |
| Recruitment | n.a. |
| Ethics oversight | n.a. |

Note that full information on the approval of the study protocol must also be provided in the manuscript.

# Field-specific reporting

Please select the one below that is the best fit for your research. If you are not sure, read the appropriate sections before making your selection.

☒ Life sciences ☐ Behavioural & social sciences ☐ Ecological, evolutionary & environmental sciences

For a reference copy of the document with all sections, see nature.com/documents/nr-reporting-summary-flat.pdf

# Life sciences study design

All studies must disclose on these points even when the disclosure is negative.

| | |
|---|---|
| Sample size | Sample size was determined on the basis of a large number of previous studies using similar methods and dealing with similar proteins. An example is shown in http://www.ncbi.nlm.nih.gov/pubmed/23427024. |
| Data exclusions | No data was excluded from initial analysis. |
| Replication | Purification of murine and ovine supercomplexes was performed at least 5 times and all attempts of replication were successful. Activity assays (using material pooled from replicates of purification) were performed at least 5 times and all attempts of replication were successful. |
| Randomization | Randomisation was performed during cryo-EM data processing as part of gold-standard refinement (separation of data into two randomly assigned halves). For biochemical assays randomisation was not necessary as every batch of material, pooled from many mice, was considered equivalent. Thus, the experiments did not feature experimental groups and did not have covariates. |
| Blinding | Investigators were not blinded to the sample allocations because all the samples and conditions were predetermined and analysed using the same methods. |

# Reporting for specific materials, systems and methods

We require information from authors about some types of materials, experimental systems and methods used in many studies. Here, indicate whether each material, system or method listed is relevant to your study. If you are not sure if a list item applies to your research, read the appropriate section before selecting a response.

### Materials & experimental systems

| n/a | Involved in the study |
|---|---|
| ☐ | ☒ Antibodies |
| ☒ | ☐ Eukaryotic cell lines |
| ☒ | ☐ Palaeontology and archaeology |
| ☐ | ☒ Animals and other organisms |
| ☒ | ☐ Clinical data |
| ☒ | ☐ Dual use research of concern |
| ☒ | ☐ Plants |

### Methods

| n/a | Involved in the study |
|---|---|
| ☒ | ☐ ChIP-seq |
| ☒ | ☐ Flow cytometry |
| ☒ | ☐ MRI-based neuroimaging |

## Antibodies

| | |
|---|---|
| Antibodies used | Primary antibodies: anti UQCRC2 (for CIII2) 14742-1-AP from Proteintech, anti MT-CO1 (for CIV) 459600 from Invitrogen, anti SCAF1 PA5-96994 from Invitrogen and anti NDUFV3 13430-1-AP from Proteintech. Secondary antibodies: HRP-conjugated anti-rabbit IgG (ab205718, Abcam) and anti-mouse IgG (w4021, Promega) |
| Validation | UQCRC2 polyclonal antibody tested on mouse (WB and IP) and human (WB) and published for human (WB,IHC,IF), mouse (WB) and rat (WB) (information obtained from the vendor's web page https://www.ptglab.com/products/UQCRC2-Antibody-14742-1-AP.htm). COX7A2L polyclonal antibody recommended for WB, reported to be reactive against human, mouse and rat (information obtained from the vendor's web page https://www.thermofisher.com/antibody/product/COX7A2L-Antibody-Polyclonal/PA5-96994). MT-CO1 monoclonal antibody recommended for WB, ICC/IF, IHC, reported to be reactive against human, rat, mouse, and published also for zebrafish and guinea pig (information obtained from the vendor's web page https://www.thermofisher.com/antibody/product/MTCO1-Antibody-clone-1D6E1A8-Monoclonal/459600). NDUFV3 polyclonal antibody tested on HepG2 cells, human heart tissue, human liver tissue (WB), human kidney tissue (IHC), HepG2 cells (IF) and published for human samples (WB) (information obtained from the vendor's web page https://www.ptglab.com/products/NDUFV3-Antibody-13430-1-AP.htm#tested-applications).<br>In this study, both antibodies recognise the murine and ovine proteins in WB. |

## Animals and other research organisms

Policy information about studies involving animals; ARRIVE guidelines recommended for reporting animal research, and Sex and Gender in Research

| | |
|---|---|
| Laboratory animals | species: Mus musculus<br>strain: CD1<br>age: c.a. 12 to 20 weeks<br>sex: male and female |
| Wild animals | No wild animals were used in the study |
| Reporting on sex | Findings are assumed to apply to both sexes, as respiratory supercomplexes are fundamental components of mitochondria in mammals. The starting material originated from a mixture of male and female animals and the data was not sex-disaggregated |
| Field-collected samples | No field-collected samples were used in the study |
| Ethics oversight | Ovine hearts from which the supercomplexes were purified were obtained from a local abattoir, hence no ethics approval was required.<br>For murine samples, animal treatments were performed in accordance with the Austrian "Tierversuchs-Verordnung 2012 -TVV2012 (522. Verordnung)- Methoden our Totung von Tieren", corresponding to the Annex IV (Methods of Killing Animals) of the European directive 2010/63/EU. Without any prior procedure, animals were sacrificed by cervical dislocation and hearts removed (procedure referred to as "organ removal"). According to the laws in Austria no further approval by the Federal Ministry of Austria for Education, Science and Research was needed. |

Note that full information on the approval of the study protocol must also be provided in the manuscript.